

Robust Persistence Homology Through Amplitude-Phase Separation in Persistence Landscapes

James Matuk

Department of Statistical Science
Duke University
Durham, NC, USA
james.matuk@duke.edu

Sebastian Kurtek

Department of Statistics
The Ohio State University
Columbus, OH, USA
kurtek.1@stat.osu.edu

Karthik Bharath

School of Mathematical Sciences
University of Nottingham
Nottingham, UK
Karthik.Bharath@nottingham.ac.uk

Abstract

Persistence homology of a point cloud sampled from a manifold embedded in \mathbb{R}^d using geometric filtered complexes, such as Rips or Čech complexes, is sensitive to scaling, sampling variability, and geometric configurations of the points in \mathbb{R}^d relative to the manifold. This can result in markedly different persistence diagrams for point clouds sampled from topologically identical manifolds. In this paper, we propose a practical solution to this problem by determining transformations of points in persistence diagrams, which act as a denoising mechanism by amplifying the topological signal. The transformations are obtained by computing phase functions that align the corresponding persistence landscapes, which are in bijection with the diagrams. We view persistence landscapes as piecewise linear parameterized closed curves, and carry out amplitude-phase separation using an elastic Riemannian metric. We are thus able to compute a mean persistence landscape that better preserves the overall shape of landscapes in the sample. The estimated phase functions are tied to the resolution parameter that determines the filtration of simplicial complexes used to construct persistence diagrams. For a dataset obtained under geometric, scale and sampling variabilities, the phase function prescribes an optimal rate at which to increase the radii of balls to ensure that the simplicial complex adapts to local scale changes that arise due to scale, sampling and geometric variabilities. We demonstrate benefits of our approach through several simulated examples, a semi-synthetic data example concerning cancer cells, and a real data example concerning structure of brain artery trees.

Keywords – topological data analysis, persistence landscapes, amplitude-phase separation, simplicial filtration, resolution parameter

1 Introduction

Persistence homology is a prominent tool within Topological Data Analysis (TDA) that provides a multi-resolution view of the topological features of data. As a resolution parameter changes, so do the features of the data, and these changes are recorded in persistence diagrams. Statistical analysis of samples of persistence diagrams are based on distances, such as the Wasserstein distance or bottleneck distance, which enable computation of descriptive statistics (Mileyko et al. 2011, Turner et al. 2014, Wasserman 2018) and confidence regions (Fasy et al. 2014). Carrying out TDA directly on the space of persistence diagrams is difficult since they are multisets of planar points. This motivates using functional representations of diagrams, or functional summaries, that are more amenable for statistical analysis (Berry et al. 2020) using tools from functional data analysis (Ramsay & Silverman 2005). In this paper, we will focus on persistence landscapes (Bubenik 2015), although it will become clear that the proposed method of analysis can be used on other functional summaries, such as silhouettes (Chazal et al. 2014), density estimates (Anirudh et al. 2016), rank functions (Robins & Turner 2016), persistence entropy functions (Atienza et al. 2020), persistence intensity functions and images (Chen et al. 2015, Adams et al. 2017), with suitable modifications.

For point cloud data in \mathbb{R}^d generated from a distribution with support on a lower-dimensional manifold M , persistence diagrams are typically computed by constructing geometric simplicial complexes based on an open cover of metric balls centered at data points with respect to the Euclidean distance on \mathbb{R}^d . The construction engenders noise in persistence diagrams that is complementary to the topological signal in the point cloud, since distances between data points in \mathbb{R}^d are sensitive to, mainly, three choices: (i) arbitrary (global) scaling of the point cloud; (ii) geometric configuration of the point cloud in \mathbb{R}^d with respect to the manifold M ; (iii) sampling variability, or density, of the points. The choices are linked to an implicit geometry of M : they imply an embedding $M \hookrightarrow \mathbb{R}^d$, under which a diffeomorphism of M , which preserves its topology, affects distances between points in M when measured using the Euclidean distance in the image of the embedding in \mathbb{R}^d . This results in different persistence diagrams for point clouds sampled from topologically identical manifolds M . Since the map that takes a persistence diagram to a persistence landscape is invertible Bubenik (2015), it is natural to query how such ‘topological’ noise manifests in a persistence landscape, and whether it is possible to exploit structure of the space of landscapes to mitigate noise and amplify the topological signal.

There are two main sources of variation in a functional dataset consisting of persistence landscapes: amplitude or shape¹, which captures y -axis variation, and phase, which tracks variation in the relative timing of shape features, e.g., extrema. In functional data analysis, the perils of not accounting for both sources of variation when computing summaries such as the mean or exploring dominant directions of variation via (functional) principal component analysis (PCA) are well-documented (see e.g., Marron et al. 2015, Srivastava & Klassen 2016). It is easy to see that such perils plague analysis of persistence landscapes, when viewed as points in a Banach space equipped with the L^p norm: the pointwise mean of a sample of persistence landscapes can fail to be one, and this affects interpretability of the corresponding persistence diagram. Instead, computing a mean landscape using only the amplitude components of a sample of landscapes by registering, or aligning, them will better preserve shape, and mitigate effects of topological noise.

We refer to topological noise as any variation in the data that is complementary to topological information, although we emphasize that the terminology does not imply that geometric features resulting from the above-mentioned choices are of no use in downstream statistical tasks. The situation is similar in spirit to Kendall’s definition of landmark shape as all geometric information that remains after accounting for translation, scale and rotation variabilities Kendall (1984); in this setting, position, global scale and orientation of a set of landmark points are viewed as variation complementary to geometric shape. However, in many applications, these features of an object may be valuable descriptors Kurtek et al. (2012). Thus, the main focus in Kendall’s shape analysis lies in separating geometric shape information from the other sources of variability, and using them as complementary features of landmark configurations in downstream analyses. From this perspective, in the present setting, the only true source of nuisance variation is measurement error, which in general, is confounded with the geometric and topological information.

Given a dataset X , the persistence landscape $\Lambda_X = \{\lambda_k : I \rightarrow \mathbb{R}^+; k = 1, \dots, K\}$ corresponding to a degree- p persistence diagram consists of K triangular like functions λ_k , defined on an interval I , that start and

¹The mathematical definitions of amplitude and shape are different in functional data analysis and shape analysis literature, respectively. However, since amplitude and shape features of persistence landscapes, as defined in this paper, are very closely related, we use them interchangeably.

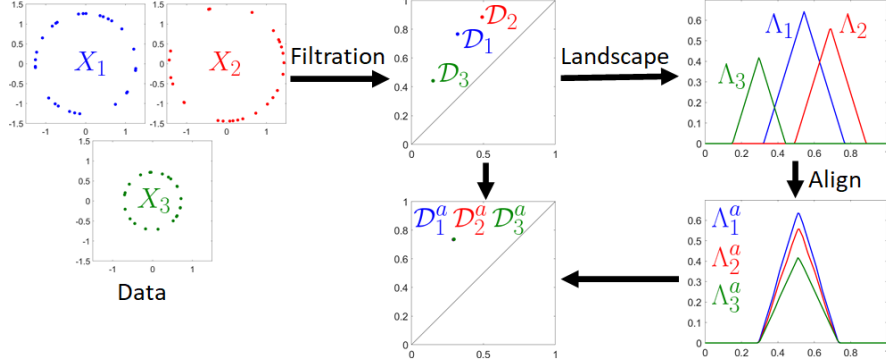


Figure 1: *Example of topological noise*: Point clouds X_1, X_2, X_3 (with different sampling) from topologically identical spaces (differing only in scale) lead to different persistence diagrams $\mathcal{D}_1, \mathcal{D}_2, \mathcal{D}_3$ and hence landscapes $\Lambda_1, \Lambda_2, \Lambda_3$. *Our approach*: Construct aligned landscapes $\Lambda_1^a, \Lambda_2^a, \Lambda_3^a$; use alignment information to get transformed/denoised diagrams $\mathcal{D}_1^a, \mathcal{D}_2^a, \mathcal{D}_3^a$; use aligned diagrams/landscapes for further statistical analysis.

end at zero. We thus view Λ_X as a parameterized closed curve in \mathbb{R}^K , and obtain curves $\Lambda_{X_i}, i = 1, \dots, n$ as landscapes from n datasets. Our main contributions are as follows.

1. We establish an explicit link between the rate of increase of the resolution parameter t in a simplicial filtration that generates a persistence diagram and magnitude of phase variation present in the component functions λ_k , as captured through a reparameterization $s \mapsto \gamma(s)$ of the curve $\Lambda_X(s)$. Specifically, we show how γ is related to variation in persistence diagrams induced by (i) arbitrary (global) scaling of the data (Figure 2), and (ii) sampling variability of data (Figure 3).
2. We show how alignment of landscapes $\{\Lambda_{X_i}\}$ by determining optimal reparameterizations $\{\gamma_i\}$ leads to a mean (average) landscape that better preserves the structure of the sample of landscapes. This induces a separation of variability in persistence landscapes into amplitude or shape, which captures the topological information in a dataset, and phase, which captures leftover variation due to geometric, global scaling and sampling variabilities. A key consequence is the ‘denoising’ of points in the corresponding persistence diagrams by transforming the points using $\{\gamma_i\}$; therefore, computing persistence diagrams for datasets $\{X_i\}$ using simplicial filtrations with balls of transformed radii $\{t \mapsto \gamma_i(t)\}$ enhances topological information in the persistence diagrams (Figure 5).
3. We demonstrate the benefits of carrying out this program on simulated examples, a semi-synthetic dataset of cancer cells, also studied in Berry et al. (2020) (Figure 10), and a real dataset consisting of brain artery trees, also studied in Bendich et al. (2016) (Figure 12).

We summarize our approach through a simple example in Figure 1 using three point clouds X_1, X_2, X_3 with degree $p = 1$ and $K = 1$ -dimensional landscapes $\Lambda_1, \Lambda_2, \Lambda_3$. Topological noise is induced purely through scale (radii of circles) and sampling variabilities. Notice how transforming the diagrams $\{\mathcal{D}_i\}$ using $\{\gamma_i\}$ from alignment of $\{\Lambda_i\}$ collapses the three points to a single one (denoising), as it should be since spaces from which $\{X_i\}$ are sampled are topologically identical. In this setting, it is evident that the global scale and sampling variabilities are captured purely in the phase component of the persistence landscapes. The aligned landscapes, in turn, capture the topological information about the underlying spaces from which the data was sampled: they all contain a single maximum corresponding to a single cycle, a topological feature that arises at the same exact time across the three point clouds. Further, the aligned landscapes are identical to each other up to a uniform scaling of the function values, i.e., they have the same shape.

What is the relationship then between topological denoising of a persistence diagram and alignment of the corresponding persistence landscapes? While there are multiple factors that induce variation in a point cloud $X = \{x_1, \dots, x_N\}$, three can be readily linked to the radius or resolution parameter t of balls $\{B_{x_i}(t)\}$ used in Čech and Rips filtrations. The first one concerns scaling of X uniformly, say by a factor greater than 1. This will ensure that a topological feature in X will be discovered at a larger radius $t^* > t$; this will

also result in a birth-death pair (b, d) in the persistence diagram that has larger b and d coordinates when compared to the unscaled case, and thus shifts the location of the peak (of a component) of the persistence landscape to the right. This represents topological noise since the underlying topological signal is invariant to scaling. Matching peaks across persistence landscapes is achieved through their alignment, and the resulting phase functions γ can be used to transform the (b, d) pairs accordingly. The phase functions, in turn, capture the relative scale of each point cloud. The other two factors are closely related, and represent the sampling density of the points x_i and the overall geometry of their configuration. For example, sparser sampling relates to requiring balls with larger radius t to discover topological features, and hence results in a larger b coordinate. In all cases, alignment allows one to separate topological information, captured through the aligned landscapes or persistence diagrams, from topological noise, in the form of global scaling, sampling variation and geometry, captured through the phase components.

To the best of our knowledge, this is the first work in TDA literature to establish a concrete link between misalignment of persistence landscapes, and topological noise in persistence diagrams. However, in a certain sense, our approach in *determining* an optimal rate of increase of t , given by $\gamma(t)$, falls between the standard approach of fixing a t for each x_i and having t change with x_i , as with a multiscale approach that allows each ball $B_{x_i}(t_i)$ to have a possibly different radius t_i (Yoon & Ghrist 2020).

2 Persistence diagram and landscape

Persistence homology is a tool that tracks homological features, such as connected components (degree-0), loops (degree-1), voids (degree-2), etc., of data at different resolutions (Edelsbrunner et al. 2002). Geometric filtered complexes, such as the Vietoris-Rips, Čech and witness complexes, built on top of a Euclidean embedding space, are commonly used to carry out persistence homology. On $\mathbb{R}^d, d \geq 2$ equipped with the standard norm, if $X = \{x_1, \dots, x_N\}$ is a point cloud, a ball of radius t can be drawn around each of the points, $B_{x_i}(t)$, and the union of the balls, $\cup_{i=1}^N B_{x_i}(t)$, can be used to compute the homology. The Čech complex, $\text{Cech}(X, t)$, consists of k -simplices whose nodes have $k + 1$ many balls with a non-empty intersection. In contrast, the Vietoris-Rips complex, or just Rips complex, $\text{Rips}(X, t)$, is easier to compute and consists of k -simplices whose nodes have $k + 1$ many balls with a non-empty pairwise intersection. At each fixed radius t , the homology of the simplicial complex is a snapshot of the features of the point cloud. However, considering all radii, $t > 0$, provides a multi-resolution view of the features of the data where features are born and die at different values of t .

Persistence homology tracks the features with a persistence diagram, a function from a countable set to $\{(x, y) \in \mathbb{R}^2 | x < y\}$, consisting of birth-death pairs, (b_j, d_j) , the times at which the j^{th} feature was born and its corresponding death time. A persistence diagram is thus a multiset consisting of these points and represents a multi-resolution summary of the homology of data. For more general treatments of persistence homology and persistence diagrams, we refer the reader to Edelsbrunner et al. (2002).

Persistence landscapes are invertible functional representations of persistence homology computed from persistence diagrams (Bubenik 2015). For data $X = \{x_1, \dots, x_N\}$, let $\mathcal{D}^p(X)$ denote its degree- p persistence diagram consisting of m birth-death pairs $\{(b_j, d_j)\}_{j=1}^m$. The basic unit of persistence landscapes are triangular functions based on points in a persistence diagram,

$$\ell_j^p(t) = (t - b_j)\mathbb{I}_{\{b_j \leq t \leq \frac{1}{2}(b_j + d_j)\}} + (d_j - t)\mathbb{I}_{\{\frac{1}{2}(b_j + d_j) \leq t \leq d_j\}}. \quad (1)$$

For $k \in \mathbb{N}$, the k^{th} landscape function is defined as $\lambda_k^p(t) = k^{\text{th}} \max_{j=1, \dots, m} \ell_j^p(t)$, which is the k^{th} maximum of the triangular functions with $\lambda_k(t) = 0$ for all $k > m$ by definition. Each function λ_k^p thus begins and ends at zero. In practice, we truncate the number of landscape functions used for data analysis to the K many that have some positive values along their domain. The degree- p persistence landscape for the data X is defined as the collection of landscape functions $\Lambda_X^p(t) = \{\lambda_k^p(t)\}_{k=1}^K$. In this work, we will consider degree- p persistence landscapes of samples of datasets X_1, \dots, X_n , which we will denote simply by $\Lambda_1(t), \dots, \Lambda_n(t)$, where context will clarify the degree p .

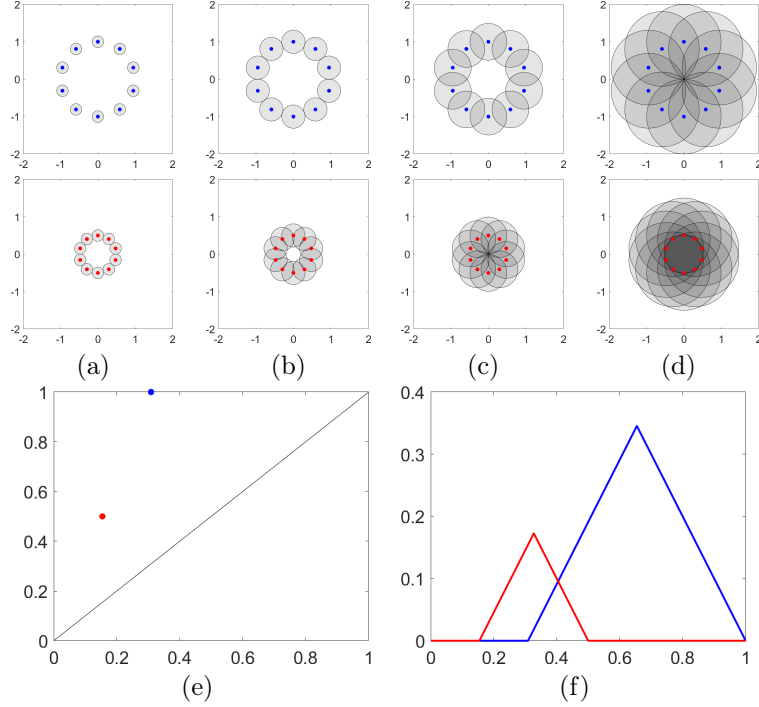


Figure 2: *Same topology with scale variability only*: Construction of Rips filtration for two point clouds on circles with radii 0.5 (red) and 1 (blue) at resolutions (a) $t = .1545$, (b) $t = .3090$, (c) $t = .5$, and (d) $t = 1$. (e) Corresponding persistence diagrams and (f) landscapes.

3 Effects of global scaling, sampling and geometric variabilities

Our interest lies in studying how changes in (i) global/local scale, (ii) geometric configurations through different choices of embeddings of M into \mathbb{R}^d , and (iii) sampling densities of points on the same manifold, result in different persistence diagrams constructed using Rips or Čech simplicial filtrations.

Consider the simple setting when the manifold M is a circle of radius $t > 0$, embedded into \mathbb{R}^2 as $\theta \mapsto (t \cos \theta, t \sin \theta)$. Note that all circles with radius $t \geq 0$ are topologically identical. However, changing the radius t changes the metric $dt^2 + t^2 d\theta^2$ on \mathbb{R}^2 , and hence its restriction to the circle; this amounts to changing the embedding that provides coordinates for the observed data points (geometric configuration), which ultimately changes the distance between points, as measured in \mathbb{R}^2 , used to construct the filtration. Figure 2 illustrates this by considering two datasets consisting of ten equidistant points along circles with radii 1 (blue) and 0.5 (red), respectively. We consider degree $p = 1$ persistence homology (loops) with $K = 1$ -dimensional landscapes when topological noise is entirely due to scale effects. In Figure 2(a)-(d), balls of different radii t are drawn around the points in the point clouds. In (a), when $t = .1545$, a loop forms for the red point cloud, while there is no loop present for the blue point cloud. In (b), when $t = .3090$, a loop forms for the blue point cloud, and the loop persists for the red point cloud. In (c), when $t = .5$, the loop closes for the red point cloud, and persists for the blue point cloud. Finally, in (d), when $t = 1$, the loop closes for the blue point cloud. The loops can be summarized by the birth-death pairs $(.1545, .5)$ and $(.3090, 1)$ for the red and blue point clouds, respectively. Panel (e) shows them in the persistence diagram, while panel (f) displays the corresponding misaligned persistence landscapes.

In the persistence diagram, (b, d) coordinates of the red point are half of those for the blue, and this matches the ratio of the radii of the two circles; this implies that the persistence landscape for the red point cloud is shorter and shifted to the left by a commensurate amount as compared to the landscape for the blue point cloud. This scale-induced topological noise thus arises by a common scaling of the triangular functions ℓ_j^1 , for each $j = 1, \dots, m$, given by

$$\ell_j^1(t) = (t - \alpha b_j) \mathbb{I}_{\{\alpha b_j \leq t \leq \frac{\alpha}{2}(b_j + d_j)\}} + (\alpha d_j - t) \mathbb{I}_{\{\frac{\alpha}{2}(b_j + d_j) \leq t \leq \alpha d_j\}}, \quad (2)$$

where $\alpha = 2$ (when blue point cloud is derived from the red). If $\alpha \in (0, 1)$, the triangular functions will be shifted to the left along the domain and will be shorter relative to $\alpha = 1$. If $\alpha > 1$, the functions will be shifted to the right and taller relative to $\alpha = 1$ (as seen in Figure 2(f)).

In this example based on the one-dimensional circle, we are able to explicitly link topological noise to a single parameter, the radius t of the circle, which governs the magnitude of both scale and geometric configuration of points. In essence, *when topological noise is due to scaling, alignment of peaks of the persistence landscapes will move points in a persistence diagram toward each other, and thus amplify the topological signal*. In other words, such topological noise manifests entirely through phase variation in the landscapes. In higher dimensions, it is not possible in general to carry out this program since the restriction of the metric on \mathbb{R}^d induced by the embedding of the manifold M is more complicated. Nevertheless, we demonstrate through several numerical examples in Section 5 that alignment of persistence landscapes acts as a denoising mechanism for the corresponding diagrams, even when topological noise is not only due to scaling.

From the discussion above, it is clear that changing the embedding (e.g., $x \mapsto (x, \sqrt{t - x^2})$) would have generated similar topological noise in the persistence diagram. This of course amounts to a change in the metric which ultimately results in a change in the simplicial filtration.

When sampling variability is present (unequal and/or non-equi-spaced points on the circle), the situation can be viewed as one involving *local* scaling of the point cloud, and alignment of peaks of the landscapes will again induce points on the persistence diagrams to move toward each other (see Section 5.2, Figure 5); similar comments apply to the situation involving measurement error (points do not lie exactly on M ; see Section 5.2, Figure 5).

4 Elastic functional data analysis of persistence landscapes

The discussion in the previous section suggests alignment of persistence landscapes, by lining up peaks and valleys of the component functions, as a viable denoising mechanism for persistence diagrams. We propose to do this through shape analysis of landscapes, viewed as parameterized curves.

Our approach is based on the elastic metric to compare shapes of curves (Srivastava & Klassen 2016), based on a convenient transform of the landscape curves. Specifically, the transformation maps landscapes into a Hilbert space, where geometric computations become simplified; this stands in contrast to the Banach space setting typically used for persistence landscapes. An important consequence of this is that we are able to compute a mean landscape based on its amplitude which, in contrast to the pointwise landscape currently computed in a Banach space setting, better preserves the shape of a landscape; moreover, the Hilbert space structure provides an inner product to carry out PCA on the amplitude or shape component of landscapes, which enables one to study dominant modes of variation in the samples of point clouds.

4.1 Reparameterizing a landscape and denoising a diagram

By virtue of its definition, a landscape is parameterized by the resolution (filtration) parameter t , used to construct the Rips or the Čech simplicial filtrations, which in principle can be any positive real. In order to choose a closed interval of \mathbb{R} as a parameter domain, note that, given n persistence landscapes, there always exists an $0 < s < \infty$ such that $\Lambda_i(t) = 0$, $\forall t > s$, $i = 1, \dots, n$. Given this, one can assume, without loss of generality, the parameter domain to be the unit interval obtained through rescaling by $1/s$. Then, for each $i = 1, \dots, n$, landscape Λ_i is a K -dimensional piecewise linear parameterized closed curve $[0, 1] \ni t \mapsto \Lambda_i(t) \in \mathbb{R}^K$ with $\Lambda_i(0) = \Lambda_i(1)$. As seen in (2), this amounts to considering scaled persistence diagrams $\{(b_{i,j}/s, d_{i,j}/s)\}_{i=1, j=1}^{n, m_i}$, so that the birth-death pairs are now in $[0, 1]^2$.

Definition 1 *A persistence landscape (diagram) $\Lambda(\{(b_j, d_j)\})$ obtained by rescaling in the above manner is referred to as a scaled persistence landscape (diagram).*

We will simply henceforth refer to a scaled persistence landscape (diagram) as a persistence landscape (diagram), unless explicitly mentioned to the contrary.

Since a reparameterization of a landscape Λ preserves its image, its shape, modulo similarity transformations, is preserved. As the set of reparameterizations, consider

$$\Gamma = \{\gamma : [0, 1] \rightarrow [0, 1] : \dot{\gamma} > 0, \gamma(0) = 0, \gamma(1) = 1\},$$

where $\dot{\gamma}$ is the derivative of γ , of orientation-preserving diffeomorphisms of $[0, 1]$, which forms a group under composition. The group Γ acts on the set of landscapes from the right as function composition: $(\Lambda, \gamma) \rightarrow \Lambda(\gamma)$. Alignment of landscapes $\{\Lambda_i\}$ thus amounts to establishing correspondence between (K -dimensional) points in the images $t \mapsto \Lambda_i(t)$, achieved by determining optimal $\gamma_i \in \Gamma$ such that the collection $\{\Lambda_i(\gamma_i)\}$ is ‘optimally’ aligned, where optimality is defined with respect to a metric-based matching functional on the landscapes. For each i , γ_i represents common phase variation in the component functions $(\lambda_{1i}, \dots, \lambda_{Ki})$ of Λ_i .

Since the resolution/filtration parameter t is the parameter for a landscape when viewed as a closed curve, we observe that:

Proposition 1 *The map $\Lambda \mapsto \Phi(\Lambda) := \{(b_j, d_j)\}$ that takes a scaled persistence landscape Λ to a unique scaled persistence diagram $\{(b_j, d_j)\}$ is equivariant with respect to the action of Γ on the set of scaled persistence landscapes, i.e., $\Phi(\Lambda(\gamma)) = \gamma^{-1}\{(b_j, d_j)\} = \{(\gamma^{-1}(b_j), \gamma^{-1}(d_j))\}$.*

A useful way to think of the induced transform $\{(\gamma^{-1}(b_j), \gamma^{-1}(d_j))\}$ on a persistence diagram is as a *nonlinear local scale change* of the multiset of points that generalizes the global scale change described in (2). This attempts to reverse the effects of (i) working with rescaled persistence landscapes, and (ii) potential topological noise induced through the geometric construction of simplicial filtrations. Indeed, this is tantamount to considering a geometric Čech or Rips filtration with parameter $\gamma(t)$: for a point cloud X , the corresponding Rips simplicial complex then is defined as

$$\begin{aligned} \sigma = [x_1, \dots, x_k] \in \text{Rips}(X, \gamma(t)) &\iff |x_i - x_j| \leq \gamma(t) \\ &\iff \gamma^{-1}(|x_i - x_j|) \leq t, \quad \forall i, j, \end{aligned}$$

since γ is strictly increasing. Equivalently, the equivariant action on Φ implies that the metric induced by the Euclidean norm $|\cdot|$ on \mathbb{R}^d is deformed by a diffeomorphism γ^{-1} in order to track the local scale changes needed to preserve the integrity of the topological signal in the presence of topological noise.

However, some care is needed with this interpretation since $\gamma^{-1}(|\cdot|)$ fails to be a metric on \mathbb{R}^d if the function γ^{-1} is not concave, since the triangle inequality will otherwise not be satisfied. Moreover, the chain of inclusions

$$\text{Rips}(X, t') \subset \check{\text{Cech}}(X, t) \subset \text{Rips}(X, t), \text{ whenever } \frac{t}{t'} \geq \sqrt{\frac{2d}{d+1}}$$

that characterise Rips and Čech complexes with parameter t (Silva & Ghrist 2007) need not be preserved under $\gamma(t)$ for all $\gamma \in \Gamma$; since preservation would depend on the magnitude of the derivative of γ , it is difficult to provide a lower bound for $\gamma(t)/\gamma(t')$ that holds for *all* $\gamma \in \Gamma$. In principle, it is possible to restrict attention to a subset of diffeomorphisms γ with a concave inverse that preserve the chain of inclusions, but this may restrict how well one is able to denoise persistence diagrams by aligning persistence landscapes.

We can summarize the practical consequence of the above discussion in the following manner: on point clouds $\{X_i\}$, the equivariant action of Γ ensures that, in the optimally aligned landscapes $\{\Lambda_i(\gamma_i)\}$, the extrema (mainly peaks) of the component functions $(\lambda_{1i}(\gamma_i), \dots, \lambda_{Ki}(\gamma_i))$ line up, and the transformed points $\{(\gamma_i^{-1}(b_{ij}), \gamma_i^{-1}(d_{ij}))\}$, consequently, will tend to cluster, the number of which will depend on the topology of the underlying manifold. As a consequence, if Čech or Rips filtration for dataset X_i is constructed with balls of radius $\gamma(t)$, the corresponding persistence diagram will be ‘denoised’.

4.2 Optimal reparameterizations, mean amplitude landscape and PCA

The program described above rests on determining the optimal reparameterizations $\{\gamma_i\}$ from observed landscapes $\{\Lambda_i\}$. In principle, any registration or alignment procedure for curves in \mathbb{R}^K can be used. Our choice is based on the highly successful Elastic Functional Data Analysis (EFDA) framework based on a Riemannian-geometric approach based on the elastic metric for curves in \mathbb{R}^K . This framework is characterized by two important theoretical considerations for the curve alignment problem: (i) isometry, i.e., invariance to simultaneous reparameterization of curves, and (ii) invariance of optimal reparameterizations to rescaling of curves. These are addressed through the use of the elastic Riemannian metric for comparing absolutely continuous curves, which is difficult to compute in practice. For ease of exposition, we refrain from providing the definition of the metric and its properties, and refer to Chapter 10 of Srivastava & Klassen (2016) for details.

Let \mathcal{F} denote the space of all absolutely continuous curves in \mathbb{R}^K equipped with the elastic metric. Practical use of the metric is greatly simplified through use of the square-root velocity function (SRVF) representation. For any curve $\beta \in \mathcal{F}$, its SRVF is defined as

$$\beta(t) \mapsto Q(\beta(t)) = q(t) := \dot{\beta}(t)(|\dot{\beta}(t)|)^{-1/2},$$

where $\dot{\beta}(t)$ is the component-wise derivative and $|\cdot|$ is the Euclidean norm on \mathbb{R}^K . The map $Q : \mathcal{F} \rightarrow \mathbb{L}^2([0, 1], \mathbb{R}^K)$ is a homeomorphism (Bruveris 2015) with inverse $\beta(t) = \int_0^t q(u)|q(u)|du$, and effectively ‘flattens’ the complicated elastic metric: the distance $d(\beta_1, \beta_2)$ between two absolutely continuous curves with respect to the elastic metric equals $\|Q(\beta_1) - Q(\beta_2)\|_2 = \|q_1 - q_2\|_2 = [\int_0^1 |q_1(t) - q_2(t)|^2 dt]^{1/2}$, and the standard \mathbb{L}^2 metric on SRVFs of curves possesses desiderata (i) and (ii) mentioned above.

Absolute continuity of a curve in \mathbb{R}^K is defined via absolute continuity of its one-dimensional component functions. Absolutely continuous functions in one dimension have constant speed parameterization (Stein & Shakarichi 2005). In the present setting, persistence landscapes $\Lambda : [0, 1] \rightarrow \mathbb{R}^K$ are piecewise linear curves. It is known that the set of piecewise linear curves in \mathbb{R}^K is dense in \mathcal{F} (Lahiri et al. 2015), and continuity of the map Q ensures that its image under Q , consisting of piecewise constant SRVFs, is dense in $\mathbb{L}^2([0, 1], \mathbb{R}^K)$.

Our definition of the amplitude (shape) of a curve and subsequent statistical analysis approach are analogous to the definitions presented in Srivastava et al. (2011) for univariate functions. The group Γ acts on \mathcal{F} through composition, and since the map $Q : \mathcal{F} \rightarrow \mathbb{L}^2([0, 1], \mathbb{R}^K)$ is bijective, the action $(q, \gamma) = Q(\Lambda(\gamma)) = (q(\gamma))\sqrt{\gamma}$ of Γ can be defined on $\mathbb{L}^2([0, 1], \mathbb{R}^K)$, under which, the amplitude of a landscape Λ is its orbit

$$[q] := \{(q, \gamma) \mid \gamma \in \Gamma\}. \quad (3)$$

Since $\|(q, \gamma)\| = q$ for every $q \in \mathbb{L}^2([0, 1], \mathbb{R}^K)$ and $\gamma \in \Gamma$, we note that Γ acts by isometries on $\mathbb{L}^2([0, 1], \mathbb{R}^K)$. Under this definition, two curves Λ_1, Λ_2 , have the same amplitude (shape) if their corresponding SRVFs are in the same orbit, or equivalence class, i.e., there exists a $\gamma \in \Gamma$ such that $q_1 = (q_2, \gamma)$. The set of all orbits forms a partition of \mathcal{Q} and is the quotient space \mathcal{Q}/Γ . Hence, \mathcal{Q}/Γ defines the amplitude space of persistence landscapes.

The amplitude distance between two landscapes $\Lambda_1, \Lambda_2 \in \mathcal{F}$ is defined as the distance between their corresponding SRVF orbits $[q_1], [q_2] \in \mathcal{Q}/\Gamma$:

$$d_a(\Lambda_1, \Lambda_2) = d([q_1], [q_2]) = \min_{\gamma \in \Gamma} \|q_1 - (q_2, \gamma)\|_2. \quad (4)$$

Key to the definition of the above distance is the invariance of the \mathbb{L}^2 metric, under the SRVF representation, to simultaneous reparameterization of curves. The function

$$\gamma^* = \operatorname{argmin}_{\gamma \in \Gamma} \|q_1 - (q_2, \gamma)\|_2$$

is then the optimal reparameterization of Λ_2 to register or align it to Λ_1 . Furthermore,

$$\gamma^* = \operatorname{argmin}_{\gamma \in \Gamma} \|q_1 - (q_2, \gamma)\|_2 = \operatorname{argmin}_{\gamma \in \Gamma} \|c_1 q_1 - (c_2 q_2, \gamma)\|_2, \quad c_1, c_2 \in \mathbb{R}_+,$$

i.e., rescaling of the curves does not alter the optimal reparameterization.

Remark 1 *The amplitude distance $d_a(\Lambda_1, \Lambda_2)$ between two persistence landscapes is not directly comparable to any \mathbb{L}^p distance used for landscapes, since the map Q is nonlinear. It is hence difficult to study stability of amplitudes of persistence landscapes, equipped with d_a , relative to the bottleneck distance on persistence diagrams.*

Remark 2 *Strictly speaking, definitions of the amplitude distance d_a and optimal reparameterization γ^* require closing the orbits $[q]$ (under the \mathbb{L}^2 metric); without this, the amplitude distance d_a may be zero for distinct orbits, mainly since the minimal element of Γ using which d_a is defined might not exist. In Lahiri et al. (2015), it was shown that closures of the orbits are themselves equivalence classes, and d_a thus defined on the closures is a proper metric. On the other hand, in the same paper, the authors proved that, for piecewise linear curves Λ_1 and Λ_2 , there exist orbit representatives that realize the minimum of the functional*

$\tilde{\Gamma} \times \tilde{\Gamma} \ni (\gamma_1, \gamma_2) \mapsto \|(q_1, \gamma_1) - (q_2, \gamma_2)\|_2$, where equivalence classes, or amplitudes, are now defined with respect to the semigroup

$$\tilde{\Gamma} = \{\gamma : [0, 1] \rightarrow [0, 1] \text{ is absolutely continuous, } \gamma(0) = 0, \gamma(1) = 1, \dot{\gamma} \geq 0\},$$

and an algorithm was provided to determine an exact matching between the two curves. Although elegant, we do not use the exact algorithm in this work since in our setting it is necessary that the optimal reparameterization be invertible in order to be able to denoise a persistence diagram.

Denoising persistence diagrams from point clouds X_1, \dots, X_n requires determining optimal reparameterizations $\gamma_1, \dots, \gamma_n$ that *jointly* align persistence landscapes $\Lambda_1, \dots, \Lambda_n$. This requires a template landscape to align the individual ones to. We use a data-driven template given by the mean amplitude landscape. Denote by q_1, \dots, q_n the SRVFs of $\Lambda_1, \dots, \Lambda_n$. The elastic Karcher mean, or simply mean, is defined as the quantity that minimizes the sum of squared amplitude distances:

$$[\hat{\mu}_q] = \underset{[q] \in \mathcal{Q}/\Gamma}{\operatorname{argmin}} \sum_{i=1}^n \min_{\gamma \in \Gamma} \|q - (q_i, \gamma)\|_2^2. \quad (5)$$

An orbit representative $[\hat{\mu}_q]$ is found by iteratively aligning q_1, \dots, q_n to the current estimate of the mean and averaging the aligned SRVFs to produce a new mean estimate; this is repeated until convergence. For identifiability, we use the center of the orbit of $[\hat{\mu}_q]$ as the representative element of the elastic mean; henceforth, we simply refer to this element of the mean orbit as $\hat{\mu}_q$. For additional algorithmic details and the orbit centering step, we refer the interested reader to Srivastava et al. (2011). The corresponding mean amplitude landscape $\hat{\mu} \in \mathcal{F}$ is defined as $Q^{-1}(\hat{\mu}_q)$.

The joint alignment of $\Lambda_1, \dots, \Lambda_n$ can then be achieved via pairwise alignment of each Λ_i , $i = 1, \dots, n$ to the mean $\hat{\mu}$ using (4) by determining the optimal reparameterizations

$$\gamma_i = \underset{\gamma \in \Gamma}{\operatorname{argmin}} \|\hat{\mu}_q - (q_i, \gamma)\|_2, \quad i = 1, \dots, n,$$

which can be used to study phase variability. Details of methods for statistical analysis of reparameterization functions, including computation of a distance, averaging and PCA are available in Tucker et al. (2013), and are omitted here for brevity.

Since the aligned curves $\Lambda_i(\gamma_i)$, $i = 1, \dots, n$, or equivalently their SRVFs, (q_i, γ_i) , $i = 1, \dots, n$, describe amplitude (shape) variability in the sample, a sample amplitude covariance function can be defined as

$$\widehat{C_q}(t, u) := \frac{1}{n-1} \sum_{i=1}^n ((q_i, \gamma_i)(t) - \hat{\mu}_q(t))((q_i, \gamma_i)(u) - \hat{\mu}_q(u))^\top. \quad (6)$$

Amplitude-based PCA is carried out via eigendecomposition of $\widehat{C_q}(t, u)$,

$$\widehat{C_q}(t, u) = \sum_{b=1}^{\infty} \hat{\tau}_b \hat{\phi}_b(t) \hat{\phi}_b(u)^\top, \quad (7)$$

where $\hat{\phi}_b$, $b \in \mathbb{N}$ are the primary directions of amplitude variability (amplitude PCs) and $\hat{\tau}_b$, $b \in \mathbb{N}$ are variances in the corresponding directions. Typically, one selects a finite number, B , of principal components that describe a large portion of amplitude variability. The aligned SRVFs can then be projected onto the B directions of amplitude variability with largest variance:

$$\beta_{i,b} := \int_0^1 \langle (q_i, \gamma)(t) - \hat{\mu}_q(t), \hat{\phi}_b(t) \rangle dt \quad b = 1, \dots, B, \quad i = 1, \dots, n,$$

where $\langle \cdot, \cdot \rangle$ is the Euclidean inner product in \mathbb{R}^K . The PC scores, $\beta_i = \beta_{i,1}, \dots, \beta_{i,B}$, $i = 1, \dots, n$ serve as a low dimensional Euclidean representation of the amplitude of curves. To visualize the primary directions of amplitude variability, we compute $\mathcal{F} \ni Q^{-1}(\hat{\mu}_q + \nu \sqrt{\hat{\tau}_b} \hat{\phi}_b)$, which is a curve that is ν standard deviations from $\hat{\mu}_q$ in the direction of $\hat{\phi}_b$.

5 Simulation and real data studies

In this section, we present:

1. Simulation examples which demonstrate (i) denoising of persistence diagrams, obtained under scale and sampling variabilities in the data, through alignment of landscapes, and (ii) benefits of computing the mean landscape and PC directions on the set of aligned landscapes as opposed to computing a pointwise mean with unaligned ones, as currently done in practice. The mean based on aligned landscapes is the elastic mean defined in (5).
2. A semi-synthetic data example on 2D point clouds corresponding to cell outlines for four different Gleason grades of prostate cancer (from benign to most severe). The task here is to classify the point clouds into the Gleason grades by utilizing their topological, geometric and scale features. We show that the amplitude of landscapes (topological information) is most effective in discriminating between benign and very unhealthy cells, while the phase (geometry and scale) is very effective in discriminating between all four grades. In particular, phase-based classification outperforms the standard approach, which considers the unaligned landscapes (Berry et al. 2020).
3. A real data example on 3D brain artery trees, which (i) through alignment of persistence landscapes for male and female groups, uncovers how apparent differences in the unaligned mean landscapes of the two groups can be partially attributed to a difference in scale, and (ii) confirms this finding by comparing the distributions of the total artery lengths of males and females. These substantially add to the findings in Bendich et al. (2016).

For the simulated and semi-synthetic data examples, we use the `ripsDiag` function to compute persistence diagrams using the Vietoris-Rips simplicial complex for point clouds, and the `landscape` function to compute landscapes from persistence diagrams; both functions are part of the `TDA` R package (Fasy et al. 2015). In the EFDA framework, registration, mean estimation and PCA for a sample of landscapes are implemented in MATLAB; the entire procedure requires approximately 1 minute on a standard laptop for each example. Code and data to reproduce simulated examples are available: <https://github.com/jamesmatuk/EFDA-of-Persistence-Landscapes>.

5.1 Simulated Example 1: Mean from aligned landscapes

We consider 20 point clouds, where each point cloud is generated by (i) sampling M from a Discrete-Uniform(10, 30), (ii) sampling r from $|N(1, 0.3^2)|$, and (iii) generating M points uniformly on a circle with radius r . Figure 1 shows three (from 20) point clouds along with the corresponding degree $p = 1$, $K = 1$ -dimensional landscapes. Figure 3(a) shows all 20 landscapes $\{\Lambda_i\}_{i=1}^{20}$.

The amplitude and phase variations in the landscapes are related to the variability in the radii, sample size and dispersion. Panels (b)-(f) demonstrate the benefit of alignment of landscapes $\{\Lambda_i\}$: a visually better mean (c) is obtained by using the aligned landscapes $\{\Lambda_i(\gamma_i)\}$ (b) using reparameterizations $\{\gamma_i\}$ (e); transforming points in the persistence diagram (d) using $\{\gamma_i\}$ results in denoising (f) by collapsing all points to a single one, since the topology of each of the 20 point clouds is the same.

We repeat this simulation with additive pointwise noise, i.e., for each point cloud, we independently generate additive noise from a zero-mean bivariate Gaussian distribution with covariance $r(0.1)^2 I_2$, where r is the radius of the circle that underlies the ‘noiseless’ point cloud. Two examples of point clouds and their corresponding degree $p = 1$ $K = 1$ -dimensional landscape functions are shown in panels (a)&(c) and (b)&(d) of Figure 4, respectively. The degree $p = 1$ $K = 1$ -dimensional landscape functions for all 20 point clouds are shown in panel (e). Most of the landscapes generated from the noisy point clouds are similar in shape to those from the ‘noiseless’ setting. However, sometimes there is an extremely small peak, corresponding to noise in some of the landscape functions. This is most visually apparent in panel (f), where there is an extremely small peak at $t \approx 0.25$ prior to the major peak in each landscape. Due to the small magnitude of this noise-induced feature, the addition of additive noise appears to have little effect on landscape alignment and mean computation. The mean based on aligned landscapes, visualized in panel (g), is consistent with that of a circle. There is considerable variance reduction in the denoised/transformed persistence diagram in panel (j), via reparameterizations shown in (i). Importantly, points corresponding to the main feature of the

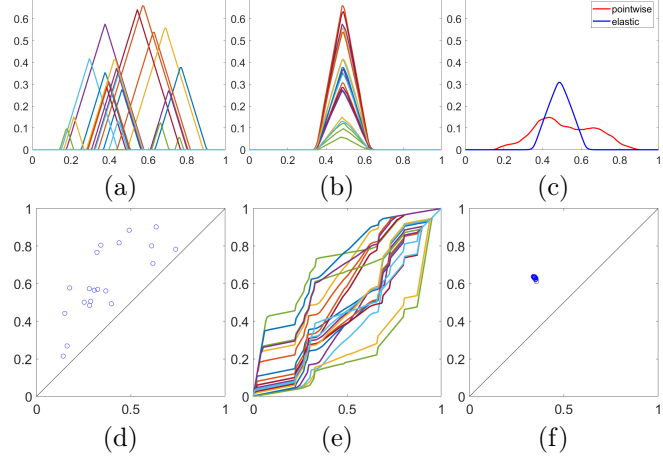


Figure 3: *Same topology with both scale and sampling variabilities*: (a) Persistence landscapes $\{\Lambda_i\}_{i=1}^{20}$ of 20 point clouds of the type in Figure 1. (b) Aligned persistence landscapes $\{\Lambda_i(\gamma_i)\}_{i=1}^{20}$. (c) Mean landscape after (blue) and without (red) alignment. (d) Noisy (rescaled) persistence diagram $\{(b_{ij}, d_{ij})\}_{i,j=1}^{20}$ from 20 point clouds. (e) Estimated phase functions $\{\gamma_i\}_{i=1}^{20}$. (f) Denoised/transformed persistence diagram $\{(\gamma_i^{-1}(b_{ij}), \gamma_i^{-1}(d_{ij}))\}_{i=1}^{20}$.

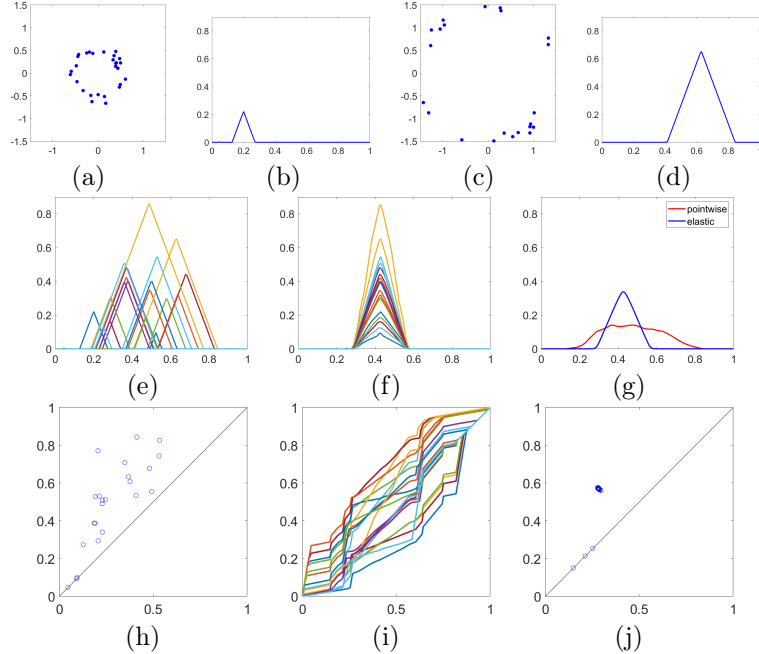


Figure 4: *Same topology with scale and sampling variabilities as well as additive noise*: (a)&(c): Two examples, from 20, of randomly generated point clouds on circles with randomly chosen radii, random sample sizes and additive noise. (b) & (d): Corresponding persistence landscapes. (e) Persistence landscapes $\{\Lambda_i\}_{i=1}^{20}$ of 20 point clouds. (f) Aligned persistence landscapes $\{\Lambda_i(\gamma_i)\}_{i=1}^{20}$. (g) Mean landscape after (blue) and without (red) alignment. (h) (Rescaled) Noisy persistence diagram $\{(b_{ij}, d_{ij})\}_{i,j=1}^{20}$ from 20 point clouds. (i) Estimated reparameterizations $\{\gamma_i\}_{i=1}^{20}$. (j) Denoised/transformed persistence diagram $\{(\gamma_i^{-1}(b_{ij}), \gamma_i^{-1}(d_{ij}))\}_{i=1}^{20}$.

data are collapsed to a single point, while points near the diagonal, corresponding to features created by the additive noise, remain near the diagonal. Such clarity is absent in the noisy persistence diagram in (h).

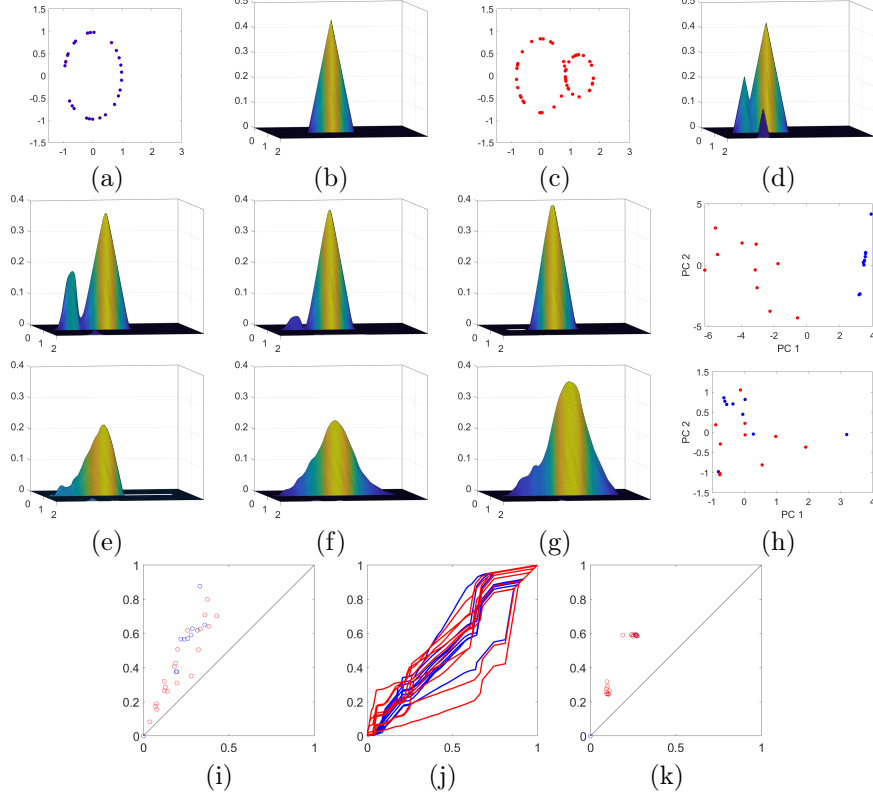


Figure 5: *Different topology with both scale and sampling variabilities*: (a) & (c) Two examples, from 20, of randomly generated point clouds from topologically different spaces (blue and red, respectively, in all relevant panels). (b) & (d) Corresponding degree $p = 1$, $K = 2$ -dimensional persistence landscapes. (e)-(g) -1, 0, 1, standard deviation from the mean landscape in the first PC direction, and (h) projection of landscapes onto the first two PC directions: following alignment (top) and without alignment (bottom). (i) Noisy and (k) denoised/transformed persistence diagrams. (j) Estimated reparameterizations.

5.2 Simulation Example: Principal component analysis on aligned landscapes

We consider a more involved setting involving 20 point clouds from two topologically different spaces: (i) one circle, and (ii) two connected circles. Point clouds from (i) are drawn in the same manner as in the previous simulation, but for the fact that sample size M is drawn from a Discrete-Uniform(20, 30). For point clouds from (ii), the radius of the larger circle is drawn from a $|N(1, 0.3^2)|$, while the radius of the smaller circle is a random proportion of the larger circle, drawn from a Beta(10, 10). Panels (a) and (c) of Figure 5 show one point cloud each from (i) and (ii).

We consider degree $p = 1$ homology and $K = 2$ -dimensional persistence landscapes $\{\Lambda_i = (\lambda_{i1}, \lambda_{i2})\}_{i=1}^{20}$. For point clouds from (i), λ_{i1} will have one peak and $\lambda_{i2} = 0$ for all t ; on the other hand, for point clouds from (ii), λ_{i1} will have two peaks and λ_{i2} will have a single peak.

Top and bottom rows of panels (e)-(g) in Figure 5 show mean landscapes and PC directions following alignment and without alignment, respectively. Panel (h) clearly highlights the benefits of alignment of landscapes through better separation of the two settings, (i) and (ii), when projected along two PC directions. Specifically, in the top row, when PCA is carried out on aligned landscapes, all of the point clouds that have two loops have a negative first PC score, while all of the point clouds with only one loop have a positive first PC score. There is no such clear separation of the two groups when PCA is performed on unaligned landscapes, as seen in the bottom row of panel (h).

Following results from the previous simulation, we expect to see two clear clusters in the denoised persistence diagram, corresponding to two distinct topological features, using reparameterizations $\{\gamma_i\}$, shown in panel (j), and this is indeed the case as seen in panel (k). This is explained as follows: points concentrated

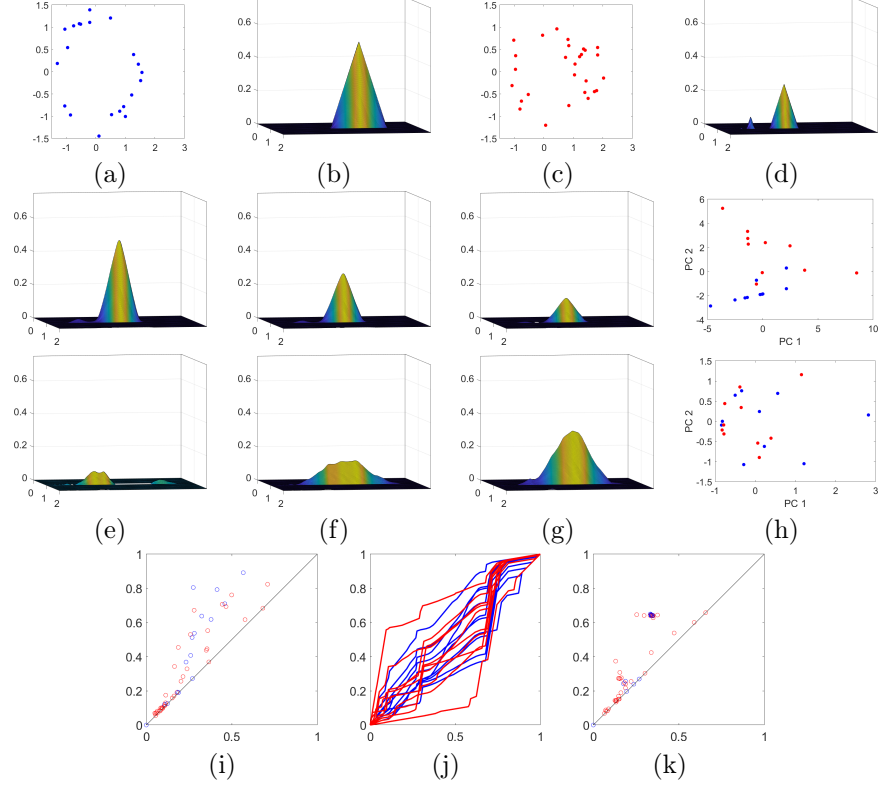


Figure 6: *Different topology with scale and sampling variabilities as well as additive noise:* (a) & (c) Two examples, from 20, of randomly generated point clouds from topologically different spaces (blue and red, respectively, in all relevant panels). (b) & (d) Corresponding degree $p = 1$, $K = 2$ -dimensional persistence landscapes. (e)-(g) -1, 0, 1, standard deviation from the mean landscape in the first PC direction, and (h) projection of landscapes onto the first two PC direction: following alignment (top) and without alignment (bottom). Noisy (i) and denoised/transformed (k) persistence diagrams. (j) Estimated reparameterizations.

around $(b, d) \approx (0.25, 0.6)$ correspond to the single circle in the blue point clouds and the large circle in the red point clouds. This is consistent with the data generating process where the large circles across the two groups correspond to each other. The points associated with the second feature for the red point clouds are concentrated around $(b, d) \approx (0.1, 0.25)$ and correspond to the additional significant homological feature (smaller circle) that generally has smaller persistence than the larger feature (larger circle). It is very difficult to discern such topological information from the noisy diagram in panel (i).

We repeat this simulation with additive noise. For point clouds in the blue group (single circle), we independently generate additive noise from a zero-mean bivariate Gaussian distribution with covariance $r(0.1)^2 I_2$, where r is the radius of the circle that underlies the ‘noiseless’ point cloud. We repeat this procedure for point clouds in the red group, but noise is generated such that the covariance depends on the radius of one of the two circles that it belongs to. A single example of a point cloud in the blue and red group are shown in Figure 6(a)&(c); the corresponding degree $p = 1$ $K = 2$ -dimensional landscapes are shown in panels (b)&(d). The shapes of the landscapes in each group are similar to those displayed in the ‘noiseless’ setting. However, here, we notice some differences in PCA carried out on aligned landscapes. The first direction of variability, viewed in the top row of panels (e)-(g) appears to be associated with scale variability in the point cloud data. On the other hand, as confirmed in the top row of panel (h), the second direction of variability appears to be associated with the homology of the point clouds, i.e., most of the red point clouds, generated from two connected circles, have a positive second PC score, while most of the blue point clouds, generated from a single circle, have a negative second PC score. Since noise can distort topological features, there does appear to be some overlap between the two classes based on the first two PC scores. This observation is in contrast

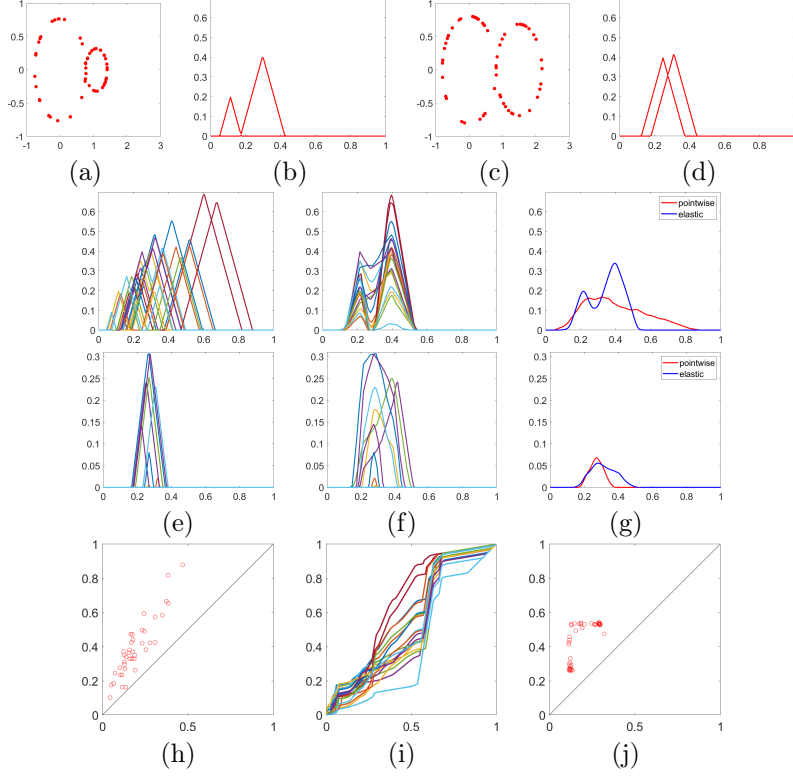


Figure 7: *Same topology with both scale and sampling variabilities:* (a)&(c) Two examples, from 20, of randomly generated point clouds. (b)&(d) corresponding persistence landscapes. With two rows corresponding to two component landscapes: (e) Persistence landscapes $\{\Lambda_i\}_{i=1}^{20}$ of 20 point clouds. (f) Aligned persistence landscapes $\{\Lambda_i(\gamma_i)\}_{i=1}^{20}$. (g) Mean landscape after (blue) and without (red) alignment. (h) (Rescaled) Noisy persistence diagram $\{(b_{ij}, d_{ij})\}_{i=1}^{20}$ from 20 point clouds. (i) Estimated reparameterizations $\{\gamma_i\}_{i=1}^{20}$. (j) Denoised/transformed persistence diagram $\{(\gamma_i^{-1}(b_{ij}), \gamma_i^{-1}(d_{ij}))\}_{i=1}^{20}$.

to the ‘noiseless’ setting, where the two classes are clearly separated based on the first PC score alone. The corresponding PC scores computed based on unaligned landscapes, shown in the bottom of panel (h), provide no such distinction between the two classes. A comparison of the denoised/transformed persistence diagram presented in Figure 6(k) to its noisy counterpart in panel (h) shows the benefits of our approach. While the clustering of features in panel (k) is not as clear as in the ‘noiseless’ setting, one can still extract useful homological information from the denoised/transformed persistence diagram. On the other hand, this is not possible based on the noisy diagram in panel (i).

5.3 Simulation Examples: Additional mean estimation examples

In Figure 7, we consider mean estimation based on degree $p = 1$ $K = 2$ -dimensional persistence landscapes computed from 20 point clouds that consist of uniformly sampled points along two circles with different radii. The point clouds in this example are generated in the same exact way as the data in the red group in the previous simulation. Panels (a) and (c) show two examples of randomly generated point clouds with their corresponding degree $p = 1$ $K = 2$ -dimensional landscapes in panels (b) and (d). Panels (e)-(g) show the $K = 1$ (top) and $K = 2$ landscape functions, their alignment, and a comparison of the mean before (red) and with (blue) alignment, respectively. The proposed alignment procedure results in a mean landscape that better preserves the major features along both landscape components. On the other hand, the unaligned mean landscape destroys the prominent two peak structure in the first component. In panel (j), the points in the denoised/transformed persistence diagram, corresponding to the two loops in the point clouds, form two separate clusters making the presence of these features in the data much clearer; the noisy diagram shown in

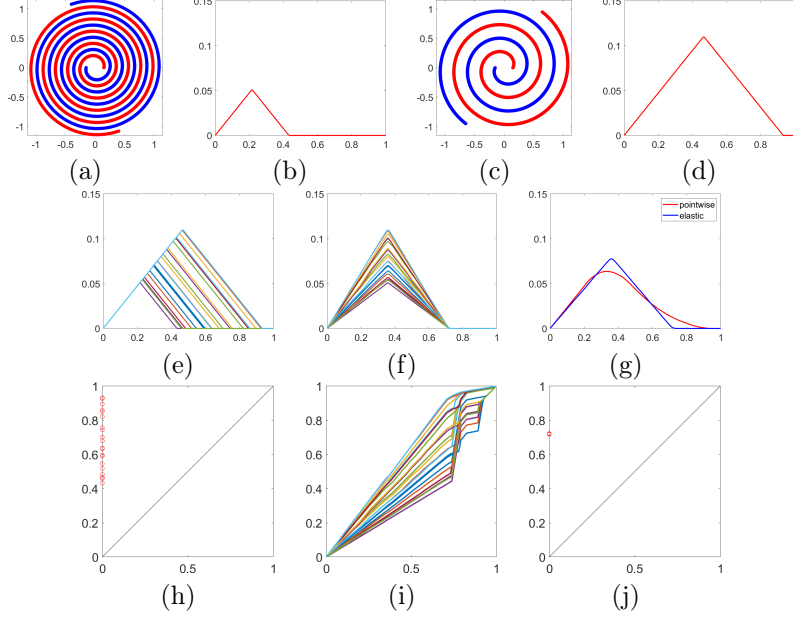


Figure 8: *Same topology with scale variability*: (a)&(c) Two examples, from 20, of randomly generated point clouds. (b)&(d) Corresponding persistence landscapes. (e) Persistence landscapes $\{\Lambda_i\}_{i=1}^{20}$ of 20 point clouds. (f) Aligned persistence landscapes $\{\Lambda_i(\gamma_i)\}_{i=1}^{20}$. (g) Mean landscape after (blue) and without (red) alignment. (h) (Rescaled) Noisy persistence diagram $\{(b_{ij}, d_{ij})\}_{i=1}^{20}$ from 20 point clouds. (i) Estimated reparameterizations $\{\gamma_i\}_{i=1}^{20}$. (j) Denoised/transformed persistence diagram $\{(\gamma_i^{-1}(b_{ij}), \gamma_i^{-1}(d_{ij}))\}_{i=1}^{20}$.

panel (h) does not provide such a distinction.

In Figure 8, we consider mean estimation based on degree $p = 0$ $K = 1$ -dimensional persistence landscapes computed from 20 point clouds that consist of 2000 points uniformly sampled along two interwoven spirals. The tightness of the spirals is random, so that the spirals complete Uniform(2, 5) revolutions. Panels (a) and (c) show two examples of point clouds generated in such a manner with their corresponding degree $p = 0$ $K = 1$ -dimensional landscapes in panels (b) and (d). The tighter spirals in panel (a) have points closer together, and the resulting landscape is smaller and shifted to the left as compared to the spirals in panel (c). When computing landscape functions, we only considered the point in persistence diagrams that corresponded to the death time that coincided with the intersection of the two spirals present in each point cloud. Panels (e)-(g) show landscapes for all 20 point clouds, their alignment, and a comparison of the mean before (red) and with (blue) alignment. The mean based on aligned landscapes appears to have sharper features that are consistent with the observed landscapes. Based on the denoised/transformed persistence diagram in panel (j), in contrast to the noisy persistence diagram in panel (h), it is evident that warping completely accounts for the scale variability associated with the tightness of the spirals, i.e., all points collapsed to a single point in the denoised/transformed persistence diagram.

In Figure 9, we consider mean estimation based on degree $p = 1$ $K = 2$ -dimensional persistence landscapes computed from 20 point clouds that consist of 1000 points sampled uniformly on a ringed torus. The major radius of each torus is sampled from a $|N(2, .3^2)|$, while the minor radius is a proportion Beta(10, 10) of the major radius. Two example point clouds are shown in panels (a) and (c). We preprocess the persistence diagrams used to compute the degree $p = 1$ $K = 2$ -dimensional persistence landscapes by disregarding all points in the persistence diagram except for the two points with longest persistence, as these points correspond to the two loops formed by the torii that underlie the point clouds. The landscapes corresponding to point clouds in (a) and (c) are shown in (b) and (d), respectively. Clearly, the estimated landscapes can vary widely depending on the relationship between the major and minor radii. Panels (e)-(g) show the first (top) and second (bottom) landscape functions, their alignment, and a comparison of the mean without (red) and after (blue) alignment. The first landscape function is automatically weighted higher during alignment due to the

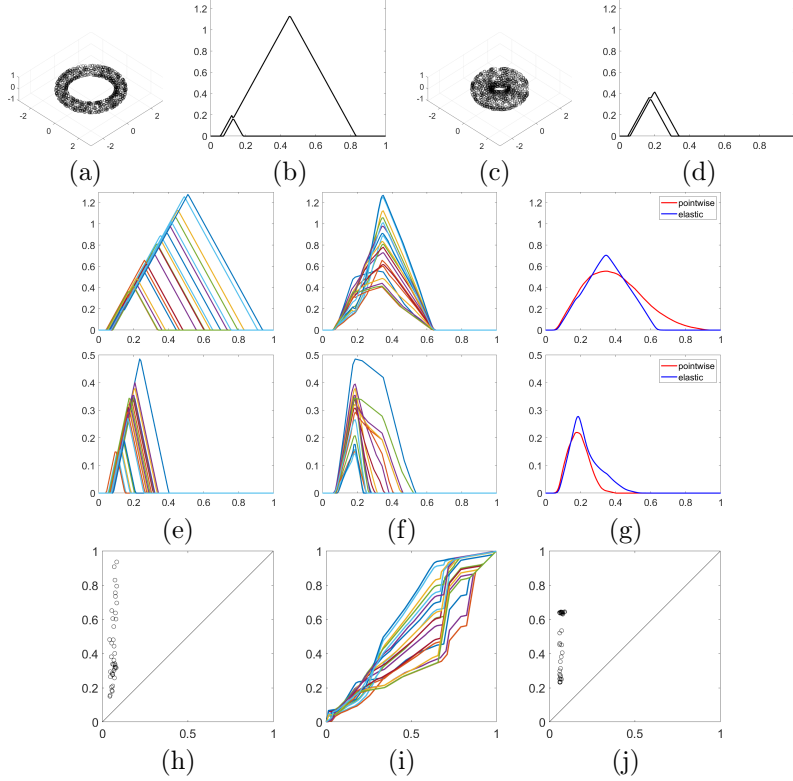


Figure 9: *Same topology with scale and sampling variabilities*: (a)&(c) Two examples, from 20, of randomly generated point clouds. (b)&(d) Corresponding persistence landscapes. With two rows corresponding to two component landscapes: (e) Persistence landscapes $\{\Lambda_i\}_{i=1}^{20}$ of 20 point clouds. (f) Aligned persistence landscapes $\{\Lambda_i(\gamma_i)\}_{i=1}^{20}$. (g) Mean landscape after (blue) and without (red) alignment. (h) (Rescaled) Noisy persistence diagram $\{(b_{ij}, d_{ij})\}_{i=1}^{20}$ from 20 point clouds. (i) Estimated reparameterizations $\{\gamma_i\}_{i=1}^{20}$. (j) Denoised/transformed persistence diagram $\{(\gamma_i^{-1}(b_{ij}), \gamma_i^{-1}(d_{ij}))\}_{i=1}^{20}$.

relatively large magnitude of the peak as compared to the second landscape function. In panel (j), the points in the denoised/transformed persistence diagram, using the reparameterizations shown in (i), concentrate to make the presence of the features more clear; the two detected features describe the two loops. In comparison, the noisy diagram shown in panel (h) does not provide a clear distinction.

5.4 Semi-synthetic Data Example: Cancer cells with different Gleason grades

As described in Berry et al. (2020), the Gleason grading system is a prognostic tool to help understand the severity of prostate cancer. Grading groups are assigned based on features of a prostate gland biopsy. In more benign biopsies, carcinoma cell walls are well-defined as seen in Figure 10(a). On the other hand, unhealthy cells lose their structure and have very irregular shapes as shown in Figure 10(b). Using a variety of functional summaries of persistence diagrams, Berry et al. (2020) classified simulated point clouds representing four different Gleason grade groups that ranged from benign to unhealthy. A representative from each of the four different classes used in their study are shown in the top row of Figure 10(c)-(f), from benign to most severe shown from left to right. The middle and bottom rows of panels (c)-(f) show the corresponding degree-1 homology persistence diagrams and landscapes, respectively. As the prognostic grade worsens, the cycle in the point clouds, corresponding to the cell outline, becomes less pronounced. This is accompanied by significant changes in geometry and scale. Thus, the benign class is characterized by a persistence landscape with a large maximum in the first landscape component function, and negligible maxima in subsequent component functions. On the other hand, the most severe class is characterized by a landscape with multiple small

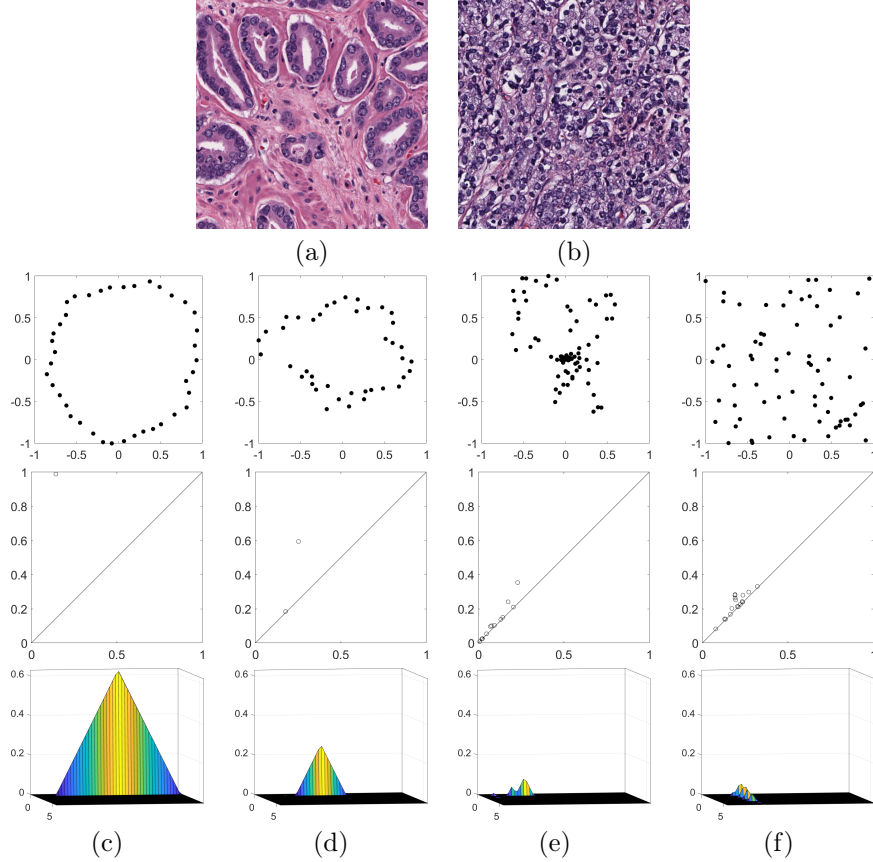


Figure 10: *Top panel. Images of prostate cancer cells (Berry et al. 2020): (a) Benign and (b) severe Gleason grade. Bottom panel. Point clouds (top row), persistence diagrams (middle row) and landscapes (bottom row) from each of the four Gleason grading scales: (c)-(f) benign to most severe.*

maxima along several landscape component functions. It is clear from this description that the landscapes contain significant shape and phase variabilities, and our aim is to classify the point clouds (landscapes) into the four Gleason grades based on these two components. In total, the data consists of 2400 point clouds with 600 classified into each of the four Gleason grades.

In particular, using this data, we study k -nearest neighbor (KNN) classification accuracy using the amplitude and phase features of the landscape curves. We also compare to one of the approaches taken in Berry et al. (2020), which applied KNN classification to the raw landscapes (without alignment). KNN classification is a distance-based approach, and we compare performance based on the following three distances:

$$\mathbb{L}^2 \text{ Distance : } d_{\mathbb{L}^2}(\Lambda_1, \Lambda_2) = \|\Lambda_1 - \Lambda_2\|_2 \quad (8)$$

$$\text{Amplitude Distance : } d_a(\Lambda_1, \Lambda_2) = \min_{\gamma \in \Gamma} \|q_1 - (q_2, \gamma)\|_2 \quad (9)$$

$$\text{Phase Distance : } d_p(\Lambda_1, \Lambda_2) = \arccos \int_0^1 \sqrt{\dot{\gamma}(s)} ds \\ \text{s.t. } \gamma = \operatorname{argmin}_{\gamma \in \Gamma} \|q_1 - (q_2, \gamma)\|_2. \quad (10)$$

The KNN classification procedure is implemented as follows. For a test observation (unknown class), we first compute the distance from this observation to each observation in a training dataset (known class). Then, we find the k nearest neighbors in the training set to the test observation, and predict its class as the one that is most frequent among the k nearest training neighbors. In case of a tie, we use the class of the nearest training neighbor. The classification accuracy is then computed as the percentage of correctly predicted classes in the test set.

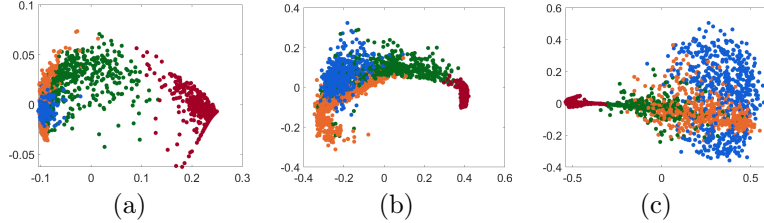


Figure 11: *Multidimensional scaling plots for the training dataset: (a) \mathbb{L}^2 distance, (b) phase distance, and (c) amplitude distance. Each point is colored according to class membership with benign = red, grade 2 = green, grade 3 = orange, and grade 4 = blue.*

| \mathbb{L}^2 | Phase | Amplitude |
|----------------|--------|-----------|
| 91% | 92.75% | 70% |

Table 1: *Classification accuracy, based on the KNN classifier, using the \mathbb{L}^2 ($k = 11$), phase ($k = 9$) and amplitude ($k = 19$) distances.*

We begin by displaying the 2D multidimensional scaling (MDS) plots, computed using the three different distances, for the training dataset. In short, MDS uses pairwise distances to compute lower-dimensional Euclidean coordinates of the data such that interpoint Euclidean distances based on these coordinates are as similar as possible to the original distances. It is evident that there is good separation between the benign (red) and Gleason grade 2 (green) classes for each of the three distances. The \mathbb{L}^2 and phase distances also provide good separation between the grade 2, grade 3 (orange) and grade 4 (blue) classes, with phase appearing more discriminative between the grade 3 and grade 4 classes. However, the amplitude distance is ineffective at separating the grade 2, grade 3 and grade 4 classes. This result is not surprising. The amplitude (shape) of persistence landscapes is effective in capturing whether and how many cycles exist in the point clouds. Thus, while it is very effective in discriminating between the benign and most severe (grade 4) classes, it does not provide effective finer classification into the four Gleason grades. On the other hand, the signal captured in the phase component is related to the size and geometry of the homological features. Visually inspecting the four point clouds in Figure 10, it is clear that these are the most discriminative features in the data. Finally, the \mathbb{L}^2 distance uses both amplitude and phase information of the landscapes without explicit control of the contribution of each component. We expect that these observations will lead to very good KNN classification rate based on the phase distance. On the other hand, the amplitude distance will only be effective at classifying benign cells versus very severe cancer.

A key question that has not yet been addressed is the choice of the number of nearest neighbors k . While we could fix this number *a priori* to some small number of neighbors, say 1 or 3, this approach will not result in optimal classification performance. Instead, we will learn an optimal k , for each of the three distances, based on training data and then apply the KNN classifier with the optimal k to testing data. Using the same training and testing split as Berry et al. (2020), data are split into 80% training (2000 landscapes, 500 in each of the four severity classes) and 20% testing (500 landscapes, 100 in each of the four severity classes). We allowed values of $k = 1, \dots, 20$. Based on KNN classification applied to the training data, we determined the optimal values of k to be 11 for the \mathbb{L}^2 distance, 19 for the amplitude distance, and 9 for the phase distance, using leave-one-out cross-validation.

We report the overall classification performance on the testing data in Table 1. The phase-based KNN classifier provides highest classification accuracy with the \mathbb{L}^2 distance-based approach in close second; the phase distance results in correct classification of 7 more cases than the \mathbb{L}^2 distance. Finally, the amplitude distance provides the lowest classification accuracy. We further report confusion matrices in Table 2. Overall, the phase distance is more effective than the other two distances in discriminating between neighboring classes, e.g., class 2 versus class 3. The amplitude distance is only effective in discriminating between the benign class and the most severe class. These observations are very similar to those reported earlier based on the MDS plots.

| | | L ² | | | | Phase | | | | Amplitude | | | |
|-----------|----------|----------------|----|----|----|-------|----|----|----|-----------|----|----|----|
| | | True | | | | True | | | | True | | | |
| | | 1 | 2 | 3 | 4 | 1 | 2 | 3 | 4 | 1 | 2 | 3 | 4 |
| Predicted | 1 | 100 | 2 | 0 | 0 | 100 | 3 | 0 | 0 | 100 | 4 | 0 | 0 |
| | 2 | 0 | 87 | 9 | 5 | 0 | 89 | 5 | 10 | 0 | 91 | 23 | 2 |
| | 3 | 0 | 8 | 86 | 4 | 0 | 4 | 94 | 2 | 0 | 5 | 77 | 86 |
| | 4 | 0 | 3 | 5 | 91 | 0 | 4 | 1 | 88 | 0 | 0 | 0 | 12 |

Table 2: *Confusion matrices for KNN classification based on the L², phase and amplitude distances.*

5.5 Real Data Example: 3D brain artery trees

We now demonstrate the utility of the proposed approach on real data of 3D point clouds representing brain artery trees discussed in Bendich et al. (2016). For a description of the experiment and data generation see Bullitt, Zeng, Gerig, Aylward, Joshi, Smith, Lin & Ewend (2005). Information regarding human subjects in the experiment is available at <http://insight-journal.org/midas/community/view/21>.

Bendich et al. (2016) computed persistence diagrams from trees which represented arteries in 98 healthy human subjects, and used persistence diagrams to compute the differences $\{d_{i,j} - b_{i,j}\}_{i=1,j=1}^{98,100}$ for subjects based on the 100 largest differences sorted from largest to smallest. Restricting focus to the largest differences serves as a denoising step, since points close to the line $b = d$ in a persistence diagram can be thought of as noise (Fasy et al. 2014).

This dataset is apt to demonstrate our approach for three reasons, one *a priori* and the other two *a posteriori*: (i) since each point cloud contains a large number (order of 10^5) of points, in order to be able to compute the diagrams, Bendich et al. (2016) subsampled 3000 points from each point cloud, thus creating large sampling variability; (ii) we uncover a significant scale effect between the two sex groups of subjects (males versus females); and (iii) we confirm the finding of Bendich et al. (2016) that there exists a significant correlation between the topological structure of the brain artery trees (as captured by PCs) and age. We note that these findings are purely exploratory and serve merely as a proof of concept for the proposed methodology.

5.5.1 Exploration of sex differences among subjects

The starting point for our analysis are the persistence diagrams available at <https://marron.web.unc.edu/brain-artery-tree-data/>, and not the original 3D point clouds. From these, we compute landscapes from degree $p = 1$ homology and $K = 100$ -dimensional persistence landscapes.

Information on the sex of each subject is also available along with the tree data. We investigate differences between mean persistence landscapes, computed from degree $p = 1$ homology persistence diagrams, grouped by sex. One major finding of Bendich et al. (2016) is the existence of sex differences in their mean degree $p = 1$ feature vectors $\{b_{ij} - d_{ij}\}$. For convenience, we denote the mean landscape for the male (female) group following alignment (within each group) by $\hat{\mu}_a^m$ ($\hat{\mu}_a^f$), and pointwise mean computed without alignment for the males (females) by $\hat{\mu}^m$ ($\hat{\mu}^f$).

The means $\hat{\mu}_a^m$ and $\hat{\mu}_a^f$ are shown in the top of Figure 12(a)-(b), respectively. The difference between the means is obtained by first aligning the group means to the common pooled mean and then taking their difference, where all operations are carried out under the SRVF representation; this difference is shown in the top row of panel (c). The bottom row of Figure 12(a)-(c) shows the pointwise means $\hat{\mu}^m$ and $\hat{\mu}^f$, and the corresponding $(\hat{\mu}^m - \hat{\mu}^f)$, when no alignment is carried out. The difference between the pointwise means has very large features. However, these features are essentially non-existent in the difference of the aligned means. *This indicates that the large difference in the pointwise means is potentially due to misalignment, and can be construed as topological noise.*

We surmise that global scale differences and sampling variability in observed data between the male and female groups may be responsible for this phenomenon. To confirm this, we use the total artery length for each subject as a measure of global scale, which is also available as part of the tree data (Bullitt, Muller, Jung, Lin & Aylward 2005). For each group, we estimated a cumulative distribution function (CDF) of total

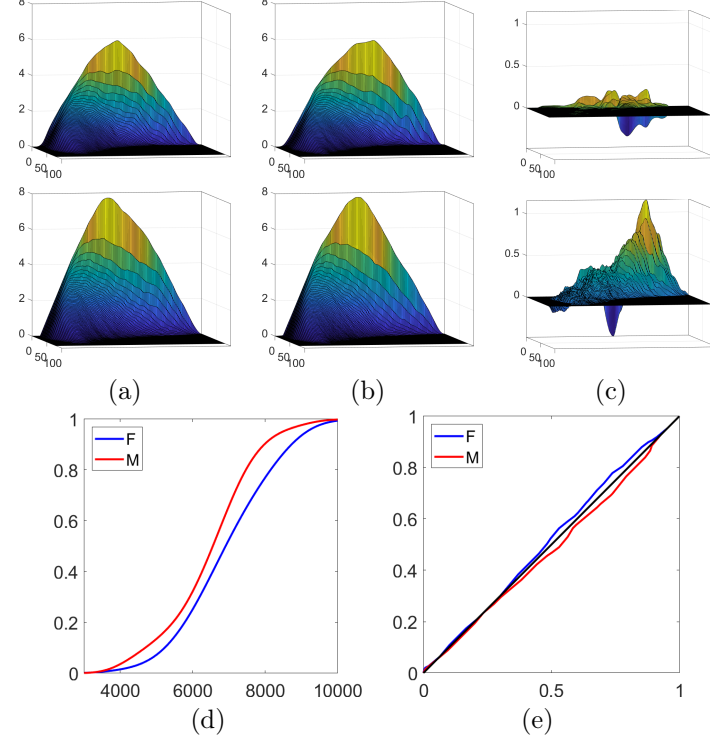


Figure 12: *Top panel.* Mean persistence landscapes and their differences for males and females in the brain artery example with (top row) and without (bottom row) alignment: (a) Female mean, (b) male mean, and (c) difference between (a) and (b). *Bottom panel.* Relationship between groupwise total artery length and relative phase of groupwise means following alignment, across sexes: (d) Estimated groupwise CDFs of total artery length, and (e) reparameterizations that align groupwise aligned means to a mean computed from alignment of the pooled data. The identity parameterization is shown in black for reference.

artery length using a kernel density estimate using the `ksdensity` function in MATLAB (default bandwidth). From the estimated CDFs shown in Figure 12(d), it appears that total artery length is stochastically ordered by sex, with females having stochastically longer brain artery trees.

Given this global scale disparity and sampling variability, we would expect $\hat{\mu}_a^f$ to be shifted to the right relative to $\hat{\mu}_a^m$. This behavior can be extracted from the phase difference between $\hat{\mu}_a^m$ and $\hat{\mu}_a^f$ to the mean computed following alignment of the pooled sample, as shown in Figure 12(e). The blue reparameterization shifts $\hat{\mu}_a^f$ to the left while the red shifts $\hat{\mu}_a^m$ to the right. The misalignment caused by differences in global scale and sampling variabilities between the two groups appear to explain the reason behind the large difference between the groupwise pointwise means.

We display three randomly chosen examples of persistence diagrams, for females and males, that were used to generate persistence landscapes, estimated reparameterizations and transformed/denoised diagrams in Figures 13 and 14. We estimated three different sets of reparameterizations during the alignment process: $\{\gamma_{i,F}\}_{i=1}^{47}$ and $\{\gamma_{i,M}\}_{i=1}^{49}$ were used to align subjects within sex to group specific means, and $\gamma_F, \gamma_{\bar{M}}$ were used to align the group specific means to a mean estimated from pooled data. In order to compare reparameterizations for subjects in different groups, we further computed the alignment of each subject to the pooled mean as $\{\gamma_{i,F}^* = \gamma_{i,F} \circ \gamma_F\}_{i=1}^{47}$ for females and $\{\gamma_{i,M}^* = \gamma_{i,M} \circ \gamma_{\bar{M}}\}_{i=1}^{49}$ for males. The corresponding results, for three randomly selected females and three randomly selected males, are shown in Figures 13 and 14, respectively; each row corresponds to a different subject. In panels (a)-(c) of each figure, we show the noisy persistence diagram, the estimated reparameterization and the denoised/transformed diagram, respectively. Regions where reparameterizations are above the identity (diagonal line $\gamma(t) = t$) correspond to regions where the inverse reparameterizations are below the identity, and vice versa. Consequently, the effect of transforming persistence diagrams for female subjects results in points in denoised/transformed diagrams that are generally smaller in magnitude than the noisy diagrams, as seen in panels (a) and (c) in Figure 13. Conversely, the

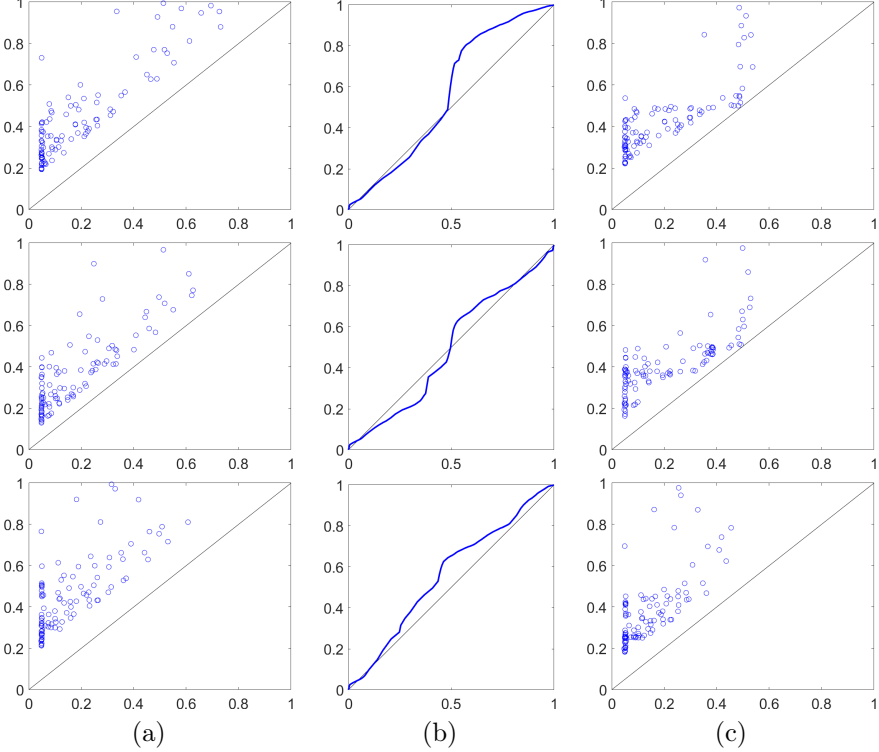


Figure 13: *Alignment results for three random subjects in the female group (each row corresponds to a different subject): (a) Noisy and (c) denoised/transformed persistence diagrams. (b) Estimated reparameterizations. The identity reparameterization is shown in black for reference.*

effect of transforming persistence diagrams for male subjects results in points in transformed diagrams that are generally larger in magnitude than the noisy diagrams, as seen in panels (a) and (c) in Figure 13. The effects of denoising are not as clear in this real data example as in the simulations. This is due to the large sampling and geometric variability across different subjects.

In summary, the above analysis suggests that the sex effect detected via pointwise analysis without alignment of the landscapes is due to global scale differences of the observed data rather than differences in homology, and thus makes a compelling case study of the perils in ignoring the distinction between, and thereby confounding of, amplitude and phase variation in landscapes.

5.5.2 Correlation between age and topological structure of brain artery trees

Bendich et al. (2016) also show that age is significantly correlated with the dominant PCs estimated using degree $p = 0$ persistence diagrams. One potential confounding variable for this relationship is total artery length, since this quantity is also significantly correlated with age as seen in Figure 15(a). To account for this, the authors first rescaled each subject's persistence diagram by their total artery length and then measured correlation between age and the dominant PCs estimated using rescaled diagrams. Even after rescaling, the relationship holds.

Here, we reanalyze the data using persistence landscapes based on the original and rescaled degree $p = 0$ persistence diagrams. As in the previous analysis, we use $K = 100$. For each case, original and rescaled, we estimate PCs using aligned and unaligned landscapes, and project onto the first two PCs to explore whether there is a correlation between either of the first two PCs and age. Panels (b)&(c) of Figure 15 show the relationship between age and the first two PCs for aligned and unaligned landscapes, respectively, estimated from the original persistence diagrams. Similarly, panels (d)&(e) of Figure 15 show the relationship between age and the first two PCs for aligned and unaligned landscapes, respectively, estimated from persistence

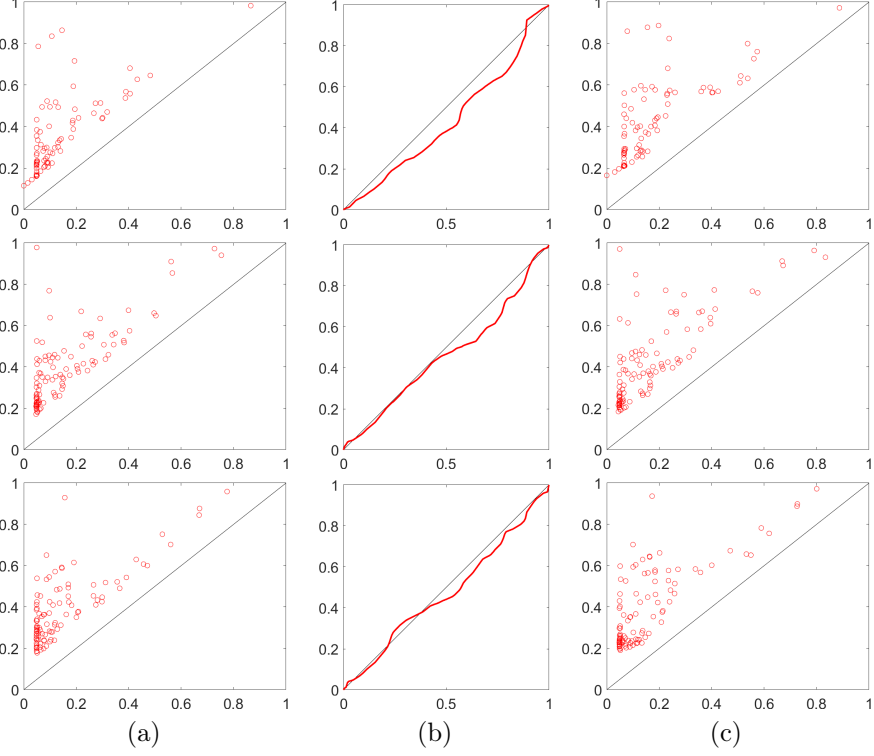


Figure 14: *Alignment results for three random subjects in the male group (each row corresponds to a different subject): (a) Noisy and (c) denoised/transformed persistence diagrams. (b) Estimated reparameterizations. The identity reparameterization is shown in black for reference.*

diagrams rescaled by total artery length. In each panel, age appears to be strongly associated with one of the first two PCs. Interestingly, the strong correlation with age is captured by the second PC estimated based on aligned landscapes computed using the original persistence diagrams. On the other hand, when aligned landscapes computed from the rescaled persistence diagrams are used to estimate the PCs, the first PC is strongly correlated with age. *Thus, based on our analysis, we are able to confirm the findings of Bendich et al. (2016). We further note that alignment of the persistence landscapes computed using rescaled persistence diagrams decreases the correlation slightly from 0.57 to 0.45 (note that the sign of the correlation coefficient is irrelevant here due to lack of directionality in the PCs); this is likely due to residual scale effects (and sampling variability) after accounting for the total artery length.*

6 Discussion

The novel approach presented in this paper can be viewed as a first step toward understanding how geometry of the manifold on which point clouds are sampled influences TDA. To see this, suppose $e : M \hookrightarrow \mathbb{R}^D$ is an equivariant embedding of a d -dimensional manifold M into \mathbb{R}^D , $D \geq d$. Then, a diffeomorphism $\phi : \mathbb{R}^D \rightarrow \mathbb{R}^D$ acts on the embedding as $\phi \circ e(M)$. The map ϕ does not change the topology of M , but constructing simplicial filtrations for point clouds under the embedding in \mathbb{R}^D using balls will transform according to ϕ since the metric is accordingly transformed; that is, for a fixed $x \in e(M)$, $\{y \in e(M) : \|x - y\|_{\mathbb{R}^D} < t\}$ will transform to $\phi(x) \in \phi \circ e(M)$, $\{\phi(y) \in \phi \circ e(M) : \|\phi(x) - \phi(y)\|_{\mathbb{R}^D} < t\}$. In the special case where ϕ corresponds to a (constant) scale change, the radius t changes nonlinearly as $t \mapsto \gamma(t)$, for a reparameterization γ , since t is forced to lie within $[0, 1]$. This phenomenon also relates to when points are sampled with variability on M , since by judiciously changing the metric depending on the locations of points, balls of different (or differently changing) radii can be used to construct the simplicial filtration, not dissimilar to the multiscale approach considered by Yoon & Ghrist (2020). Much remains to be done in this direction.

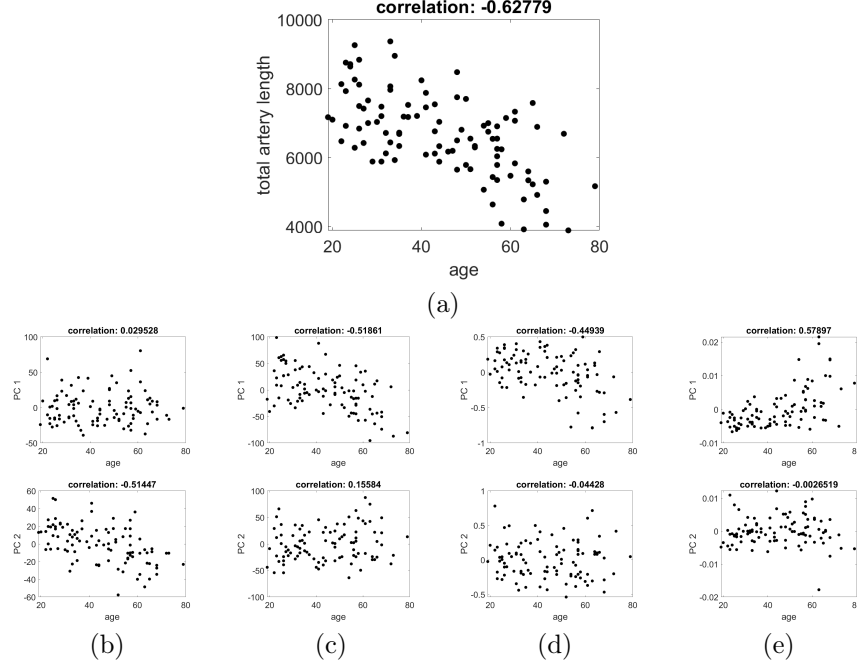


Figure 15: *Top panel.* Correlation between total artery length and age: (a) Scatterplot of total artery length versus age. *Bottom panel.* Correlation between the first two PCs estimated via aligned and unaligned landscapes and age: Scatterplots of PC 1 (top) and PC 2 (bottom) estimated using aligned (b) and unaligned (c) landscapes, computed from original persistence diagrams, versus age. Scatterplots of PC 1 (top) and PC 2 (bottom) estimated using aligned (d) and unaligned (e) landscapes, computed from rescaled persistence diagrams, versus age.

The limitations of this work inspire directions for future work. First, using scaled persistence diagrams by rescaling to $[0, 1]^2$ is also a source of topological noise, but is entirely driven by practical considerations. In principle, we could instead consider the group of diffeomorphisms of $[0, \infty)$ to align the persistence landscapes, although there would be very little phase variation for parameter values exceeding the maximum, across different point clouds, of the maximum interpoint distance within each point cloud. A compromise would be to consider the subgroup of diffeomorphisms of $[0, \infty)$ based on scaling and translating diffeomorphisms of $[0, 1]$, considered in Bryner & Srivastava (2022), to perform alignment that better reflects phase variability in the landscapes.

Second, notwithstanding the promising results for the noisy simulations, robustness of the alignment-based approach to measurement error will strongly depend on the geometry of the manifold M , sampling density and magnitude of noise in observed data on \mathbb{R}^D , especially if data have been sampled from a distribution with support only on M . One possible approach would constitute of first estimating M (and its dimension) using a manifold fitting method, and using this information to construct tailored simplicial filtrations; however, additional noise induced by the fitting procedure would have to be accounted for in downstream tasks. Another option for the large noise setting is to use explicit statistical models to align persistence landscapes that account for all sources of uncertainty. For example, Bayesian models based on shape-constraints to infer the pattern and number of extrema in landscapes may be profitably used (Matuk et al. 2021).

While the focus of this paper is on persistence landscapes, we expect our approach to be fruitful with silhouettes (Chazal et al. 2014), since similar triangular functions are used in their definition. However, feasibility of the alignment method for other functional summaries mentioned in Section 1 is not clear, and is worthy of further investigation.

Finally, for denoising a persistence diagram directly without using landscapes, it is possible to consider generalizations of the one-dimensional transforms γ of points on diagrams to the group of diffeomorphisms of \mathbb{R}^2 , along the lines of what is done in the Large Deformation Diffeomorphic Metric Mapping (LDDMM)

framework (Grenander & Miller 2007).

Acknowledgements

The MR brain images from healthy volunteers used in this paper were collected and made available by the CASILab at The University of North Carolina at Chapel Hill and were distributed by the MIDAS Data Server at Kitware, Inc. The authors would like to thank Jessi Cisewski Kehe for sharing the Gleason dataset. This research was partially funded by NIH R37-CA214955 (to SK and KB), EPSRC EP/V048104/1, and NSF DMS-2015374 (to KB), and NSF CCF1740761, NSF DMS-2015226, and NSF CCF-1839252 (to SK), and NIH R01-ES028804 (JM).

On behalf of all authors, the corresponding author states that there is no conflict of interest.

References

Adams, H., Emerson, T., Kirby, M., Neville, R., Peterson, C., Shipman, P., Chepushtanova, S., Hanson, E., Motta, F. & Ziegelmeier, L. (2017), ‘Persistence images: A stable vector representation of persistent homology’, *Journal of Machine Learning Research* **18**(8), 1–35.
URL: <http://jmlr.org/papers/v18/16-337.html>

Anirudh, R., Venkataraman, V., Ramamurthy, K. & Turaga, P. (2016), A Riemannian framework for statistical analysis of topological persistence diagrams, in ‘IEEE Conference on Computer Vision and Pattern Recognition Workshops’, pp. 1023–1031.

Atienza, N., Gonzalez-Díaz, R. & Soriano-Trigueros, M. (2020), ‘On the stability of persistent entropy and new summary functions for topological data analysis’, *Pattern Recognition* **107**, 107509.
URL: <https://www.sciencedirect.com/science/article/pii/S0031320320303125>

Bendich, P., Marron, J. S., Miller, E., Pieloch, A. & Skwerer, S. (2016), ‘Persistent homology analysis of brain artery trees’, *The Annals of Applied Statistics* **10**(1), 198 – 218.
URL: <https://doi.org/10.1214/15-AOAS886>

Berry, E., Chen, Y.-C., Cisewski, J. & Fasy, B. (2020), ‘Functional summaries of persistence diagrams’, *Journal of Applied and Computational Topology* **4**, 211–262.

Bruveris, M. (2015), ‘Optimal reparametrizations in the square root velocity framework’, *SIAM Journal of Mathematical Analysis* **48**(6).

Bryner, D. & Srivastava, A. (2022), ‘Shape analysis of functional data with elastic partial matching’, *IEEE Transactions on Pattern Analysis and Machine Intelligence* (to appear) .

Bubenik, P. (2015), ‘Statistical topological data analysis using persistence landscapes’, *Journal of Machine Learning Research* **16**(3), 77–102.
URL: <http://jmlr.org/papers/v16/bubenik15a.html>

Bullitt, E., Muller, K., Jung, I., Lin, W. & Aylward, S. (2005), ‘Analyzing attributes of vessel populations’, *Medical Image Analysis* **9**, 39–49.

Bullitt, E., Zeng, D., Gerig, G., Aylward, S., Joshi, S., Smith, J., Lin, W. & Ewend, M. (2005), ‘Vessel tortuosity and brain tumor malignancy’, *Academic Radiology* **12**, 1232–40.

Chazal, F., Fasy, B. T., Lecci, F., Rinaldo, A. & Wasserman, L. (2014), Stochastic convergence of persistence landscapes and silhouettes, in ‘ACM Symposium on Computational Geometry’, ACM, pp. 474–483.
URL: <https://hal.archives-ouvertes.fr/hal-00923684>

Chen, Y.-C., Wang, D., Rinaldo, A. & Wasserman, L. (2015), ‘Statistical analysis of persistence intensity functions’, *arXiv:1510.02502v1* .

Edelsbrunner, H., Letscher, D. & Zomorodian, A. (2002), 'Topological persistence and simplification', *Discrete & Computational Geometry* **28**(4), 511–533.
URL: <https://doi.org/10.1007/s00454-002-2885-2>

Fasy, B. T., Kim, J., Lecci, F. & Maria, C. (2015), 'Introduction to the R package TDA', *arXiv:1411.1830* .

Fasy, B. T., Lecci, F., Rinaldo, A., Wasserman, L., Balakrishnan, S. & Singh, A. (2014), 'Confidence sets for persistence diagrams', *The Annals of Statistics* **42**(6), 2301 – 2339.
URL: <https://doi.org/10.1214/14-AOS1252>

Grenander, U. & Miller, M. (2007), *Pattern Theory: From Representation to Inference*, Oxford University Press.

Kendall, D. G. (1984), 'Shape manifolds, Procrustean metrics, and complex projective spaces', *Bulletin of the London Mathematical Society* .

Kurtek, S., Srivastava, A., Klassen, E. & Ding, Z. (2012), 'Statistical modeling of curves using shapes and related features', *Journal of the American Statistical Association* **107**(499), 1152–1165.

Lahiri, S., Klassen, E. & Robinson, D. (2015), 'Precise matching of pl curves in \mathcal{C}^n in the square root velocity framework', *Geometry, Imaging and Computing* **2**(3), 133–186.

Marron, J. S., Ramsay, J. O., Sangalli, L. M. & Srivastava, A. (2015), 'Functional data analysis of amplitude and phase variation', *Statistical Science* **30**(4), 468–484.

Matuk, J., Bharath, K., Chkrebta, O. & Kurtek, S. (2021), 'Bayesian framework for simultaneous registration and estimation of noisy, sparse, and fragmented functional data', *Journal of the American Statistical Association* p. In Press.
URL: <https://doi.org/10.1080/01621459.2021.1893179>

Mileyko, Y., Mukherjee, S. & Harer, J. (2011), 'Probability measures on the space of persistence diagrams', *Inverse Problems* **27**(12), 124007.
URL: <https://doi.org/10.1088/0266-5611/27/12/124007>

Ramsay, J. O. & Silverman, B. W. (2005), *Functional Data Analysis*, Springer.

Robins, V. & Turner, K. (2016), 'Principal component analysis of persistent homology rank functions with case studies of spatial point patterns, sphere packing and colloids', *Physica D: Nonlinear Phenomena* **334**, 99–117.
URL: <https://www.sciencedirect.com/science/article/pii/S0167278916000476>

Silva, V. & Ghrist, R. (2007), 'Coverage in sensor networks via persistent homology', *Algebraic and Geometric Topology* **7**(1), 339–358.

Srivastava, A. & Klassen, E. (2016), *Functional and Shape Data Analysis*, Springer.

Srivastava, A., Wu, W., Kurtek, S., Klassen, E. & Marron, J. S. (2011), 'Registration of functional data using Fisher-Rao metric', *arXiv 1103.3817* .

Stein, E. M. & Shakarichi, R. (2005), *Real Analysis: Measure Theory, Integration, and Hilbert Spaces*, Princeton University Press.

Tucker, J. D., Wu, W. & Srivastava, A. (2013), 'Generative models for functional data using phase and amplitude separation', *Computational Statistics & Data Analysis* **61**, 50–66.
URL: <https://www.sciencedirect.com/science/article/pii/S0167947312004227>

Turner, K., Mileyko, Y., Mukherjee, S. & Harer, J. (2014), 'Fréchet means for distributions of persistence diagrams', *Discrete & Computational Geometry* **52**(1), 44–70.
URL: <https://doi.org/10.1007/s00454-014-9604-7>

Wasserman, L. (2018), ‘Topological data analysis’, *Annual Review of Statistics and Its Application* **5**(1), 501–532.

Yoon, H. R. & Ghrist, R. (2020), ‘Persistence by parts: Multiscale feature detection via distributed persistent homology’, *arXiv: 2001.01623* .